Large deformation finite element simulation of deformation and strain fields resulting from closed-end displacement pile installation in sand

S. Fu[1], Z.X. Yang[2] M.ASCE, R.J. Jardine[3] and N. Guo[4]

Abstract

Displacement piles are driven to support a wide range of structures. However, analysis of the stress and strain fields developed during their installation remains one of the most challenging problems in geotechnical engineering. Advances in design methods, particularly for sand sites, have had to rely on an imperfect analogy between pile and CPT cone penetration processes, rather than modelling pile installation itself. Recent physical model experiments provide benchmark datasets that describe the stress and deformation patterns developed around displacement piles penetrating sand masses. Following from large deformation finite element analyses that captured the stresses measured in the Grenoble 3S-R calibration chamber NE34 sand experiments, this paper presents simulations of the displacements measured in equivalent high-quality experiments conducted at Purdue University with dense, angular, #2Q-ROK silica sand. A modified Mohr-Coulomb model with state-dependent parameters was calibrated to match element tests conducted by the Authors and an Arbitrary Lagrangian-Eulerian scheme was applied in the simulations. The evolution and distribution of the deformations induced by pile penetration are compared with the experiments. Predictions for the deformation and strain fields

[1] Postgraduate student, Department of Civil Engineering, Zhejiang University, 866 Yuhangtang, Hangzhou 310058, China, 11912013@zju.edu.cn;
[2] Professor, Department of Civil Engineering, Zhejiang University, 866 Yuhangtang, Hangzhou 310058, China, zxyang@zju.edu.cn;
[3] Professor, Department of Civil and Environmental Engineering, Imperial College London, SW7 2AZ, UK, r.jardine@imperial.ac.uk;
[4] Professor, Department of Civil Engineering, Zhejiang University, 866 Yuhangtang, Hangzhou 310058, China, nguo@zju.edu.cn

applying during and after pile installation are presented, showing broad agreement between the simulations and experiments. The predicted and measured pile capacities are also compared and contrasted. Points of divergence between the simulations and tests are highlighted and their implications for numerical modelling are discussed.

Keywords: driven piles, sand, half-circular calibration chamber, finite element analysis, Arbitrary Lagrangian-Eulerian; deformation field

Introduction

Driven piles are widely employed to support high-rise towers, major bridges, offshore platforms, wind turbines and many other structures. Predicting how they perform in service is central to optimizing their safe and economic design. However, conventional axial capacity and load-displacement prediction methods have been shown to have relatively poor reliability, especially in sands. Database studies (Jardine et al. 2005; API RP2GEO 2014; Yang et al. 2015a, b, c; Yang et al. 2017; Lehane et al. 2017) show that Cone Penetration Test (CPT)-based approaches give the reliable predictions for axial capacity in sands, provided that they recognize the crucial importance on the local shaft shear resistances (available at any given depth below the ground surface) of:

- Initial sand state, as measured by local CPT q_c values which also control end bearing
- The normalized relative depth (h/R) of the pile tip below the point on the shaft
- Radial stress changes provoked by dilation involving the sand and pile roughness, which are particularly important with small model piles
- Coulomb ultimate shaft failure being achieved under loading, with critical state ultimate

angles that are independent of relative density and rise with the ratio of pile roughness to grain size.

The well performing ICP-05 (Jardine et al. 2005) and UWA-05 (Lehane et al. 2005) CPT-based methods offer coefficients of variation ≈ 0.3 when compared with measurements from high-quality pile load test databases. Routine methods for predicting displacements under monotonic or cyclic working axial and lateral loads are far less reliable (Jardine 2020). Considerably different behaviors are observed, for example, between identically sized driven and bored piles. Understanding how installation affects the stress and strain conditions developed around driven piles is essential to advancing modelling of axial load-displacement responses.

Experimental studies

Extensive research has taken place into the mechanisms that govern driven pile behavior. Although rigorous theoretical solutions are unavailable to quantify how installation affects subsequent loading behavior, field tests and calibration chamber model pile experiments provide key evidence regarding the highly non-uniform stresses and strain distributions developed during installation. The small number of reliable local stress observations made around displacement piles installed at sand sites include those reported by Lehane et al. (1993), Chow (1997) and Jardine et al. (2005). These, with calibration chamber model tests by Gavin and Lehane (2003), were influential in formulating CPT-based axial capacity procedures for sand sites; see for example Lehane et al. (1992), Chow (1997), Jardine et al. (2006). Calibration chamber experiments by Yang et al. (2010), Tsuha et al. (2012), Jardine et al. (2013a, b), Arshad et al. (2014), Rimoy et al. (2015), Tehrani et al. (2018) and Tovar-Valencia et al. (2018) have since added further valuable insights and datasets that allow benchmarking of analytical methods.

Field measurement of the deformation patterns applying around such piles remains unfeasible, but image-based analysis has been applied laboratory model investigations of pile penetration process into granular media. The studies include early X-ray film photogrammetry (Robinsky et al. 1964) and X-ray television (TV) imaging (Kobayashi and Fukagawa 2003), non-invasive X-ray computed tomography (CT) (Otani et al. 2005; Ngan-Tillard et al. 2005; Andò et al. 2012; Paniagua et al. 2013; Doreau-Malioche et al. 2018) and optical techniques, such as particle image velocimetry (PIV) (White 2002; White and Bolton 2004; Liu 2010; Mo et al. 2015) and digital image correlation (DIC) (Arshad 2014; Arshad et al. 2014; Tehrani et al. 2018; Tovar-Valencia et al. 2018). PIV and DIC studies provided the first detailed descriptions of the displacement and strain fields associated with pile (or cone) penetration in sand. Transparent soils and associated optical systems have also been employed in advanced nonintrusive three-dimensional deformation measurements (Iskander et al. 2002; Liu 2003; Lehane and Gill 2004; Ni et al. 2010).

Numerical analysis by DEM and MPM

Parallel research has taken place with numerical methods. Arroyo et al. (2011) and Butlanska et al. (2014) simulated CPT by discrete element modelling (DEM) with up-scaled particle sizes, showing good qualitative agreement with calibration chamber experiments reported by Jardine et al. (2013a, b). To simulate particle crushing and shearing banding noted in laboratory studies, Wang and Zhao (2014) introduced particle breakage mechanism into DEM simulations of steady pile penetration, finding some differences with experiments reported by Yang et al. (2010), which they ascribed to load cycling imposed during pile driving or cyclic jacking. DEM simulations of the stress regimes generated by pile installation were also reported by Liu and Wang (2016), who interpreted significant discrepancies between their results and measurements by Jardine et al. (2013a, b) as

being due to their adopted boundary conditions. Ciantia et al. (2019) reported further DEM simulations of monotonic pile penetration into crushable particles, and the non-uniform stress regime developed around the pile shaft and marked arching above the pile tip, showing average stress results that matched the experiments by Jardine et al. (2013b) reasonably well at h/R values up to ≈ 40, without reproducing fully the field trends for shaft radial effective stresses to decay further at higher h/R. However, DEM is extremely computationally expensive. The particle sizes in published studies have all been increased very considerably to enable practical run-times, while chamber diameters have been reduced at the cost of potentially suffering unwelcome boundary effects related to small chamber-to-cone diameter ratios.

The material point method (MPM) has also been applied by several authors in pile driving studies (Tehrani et al. 2016; Phuong et al. 2016; Ceccato et al. 2016; Lorenzo et al. 2018; Gao et al. 2022). Modelling the soil-pile interface remains challenging in MPM where an 'automatic' contact algorithm is usually applied that prohibits separation or slip at the shaft (Sulsky et al. 1994). Bardenhagen et al. (2000, 2001) extended the no-slip contact algorithm to a frictional contact, which was applied to model interparticle behavior in granular materials. Lemiale et al. (2010) improved the contact algorithms of Bardenhagen et al. (2001) on the treatment of contact at interfaces between rigid and deformable bodies. Nevertheless, MPM is known to suffer from difficulties including null-space errors (Tran and Sołowski 2019) and volumetric locking (Coombs et al. 2018) that can make it less accurate than FEM.

Finite Element treatments

Routine Lagrangian Finite Element (FE) analysis is not suitable for simulating pile installation as it suffers contact and mesh distortion problems when soil deformations are large. To overcome

114 these difficulties, either new contact laws or a 'rigid tube artifice' is needed to guide the installation
115 (Sheng et al. 2004; Mahutka et al. 2006; Henke 2008, 2010). Sheng et al. (2004) simulated
116 continuous in-flight centrifuge penetration of a closed-ended pile (0.03 m in diameter with a 60°
117 cone end) into dry dense sand. A large–slip frictional contact was developed and the sand was
118 modelled as drained Modified Cam Clay (MCC). Installation stress and strain contours were
119 predicted as functions of relative pile tip depth h/R but not compared with any experimental
120 measurement.

121 Algorithms are available in ABAQUS (Dassault Systèmes Simulia 2016) to facilitate large
122 deformation analyses. The code's Arbitrary Lagrangian-Eulerian (ALE) options separate the
123 material and mesh displacements to avoid mesh distortion problems, and re-meshing is used to
124 maintain mesh quality. The alternative CEL (Coupled Eulerian–Lagrangian) option in ABAQUS treats
125 the pile as rigid Lagrangian body and the soil as a Eulerian body, in which the soil can deform as
126 freely as a fluid inside the restricted mesh area, and thus avoid the mesh distortion problem. Both
127 techniques have been employed in pile penetration analyses (Zhang et al. 2013, 2014; Wang et al.
128 2015; Henke et al. 2010; Qiu et al. 2011; Ko et al. 2016). The CEL option provided in ABAQUS cannot
129 apply an upper stress-controlled boundary, as applied in the experiments modeled in this paper,
130 and can only be applied in 3D simulations. The ALE technique appears more suitable for modeling
131 the pressurized chamber tests considered; it also offers a more computationally efficient 2D
132 axisymmetric analytical option. Wang et al. (2015) and Zhang et al. (2013, 2014) applied this
133 technique to simulate calibration chamber tests' stresses measured by Yang et al. (2010) and
134 Jardine et al. (2013a, b). Noting that significant particle crushing occurs during pile installation, the
135 sand was modelled with a linear elastic breakage constitutive law. Particle breakage distribution

were successfully simulated beneath the pile tip and along the shaft and the results compared with experimental data, along with end-bearing profiles and the predictions for the stresses developed within the sand mass during the steady penetration. Their analysis predicted key aspects of the measured stresses but were not able to recover fully the observed variations with normalized pile tip depth (h/R).

Yang et al. (2020) presented ALE analyses of the highly instrumented 'Grenoble' calibration chamber tests on piles (with 5 μm centerline average roughness) reported by Jardine et al. (2013a, b). It was not feasible to apply a critical state-based boundary surface model, such as that applied by Taborda et al. (2020) to represent the test sand, nor to simulate grain crushing or the dilative local radial stress changes that occur along the shaft under axial loading. A simpler, variable parameter, Mohr-Coulomb model was calibrated against high-quality element tests conducted on the test sand over appropriate pressure ranges. Dilatancy and shearing resistance angles were varied to match the mean effective stress, plastic shear strains and void ratios applying in the sand mass at different locations and installation stages. The overall modelling capability was checked by performing predictions of the calibration chamber CPT q_c traces. Where necessary, parameters were adjusted, within reasonable bounds, to improve predictions. Numerical predictions were then advanced for the radial, circumferential, and vertical normal stresses developed during and after pile installation. The analyses showed encouraging agreement with the measurements, although no attempt was made to match the experimentally observed constrained dilative behavior at the sand-shaft interface, which was linked to the pile roughness.

Contribution and aims of this study

As summarized above, earlier numerical analyses have successfully predicted the stresses

159 measured around displacement pile installation in sand. The present study aimed to contribute
160 new analyses that attempt to match the strain fields measured by Arshad et al. (2014) in high
161 quality calibration chamber pile experiments conducted at Purdue University. The numerical
162 simulations are conducted within the same framework, but with different soils and boundary
163 conditions, to Yang et al.'s (2020) successful modeling of high-quality stress field measurements
164 made independently with another silica sand (Fontainebleu NE34) in a different calibration
165 chamber at Grenoble (France) by Jardine et al., (2013a, b).

166 The new study demonstrates that the ALE large-deformation simulation technique can, in
167 combination with a simple, variable parameter, Mohr-Coulomb model, predict the comprehensive
168 strain measurements made in the Purdue, as well as stresses in the Grenoble experiments, and
169 provide key insights into their evolution and mechanisms. The Authors are not aware of any
170 comparably comprehensive and quantitative comparisons between numerical predictions and
171 high-quality experimental measurements of displacements, strains, and stresses. These new
172 analyses show an encouraging way forward for displacement pile installation analyses as well as
173 furthering understanding that should translate into practical guidance regarding displacement pile
174 analysis and design in sand.

175

176 **ALE Finite Element analysis of calibration chamber DIC experiments**

177 This paper extended Yang et al.'s (2020) ALE stress analyses by making comparisons between
178 numerical predictions and the vertical, radial and shear displacements and strains measured in
179 independent benchmark 'half' pile calibration chamber pile penetration experiments conducted in
180 sand at Purdue University (Arshad 2014; Arshad et al. 2014).

181

Calibration chamber experiments

Foray et al. (1993, 1998), Paik et al. (2003), Gavin and Lehane (2003), White and Bolton (2004), Yang et al. (2010), Paik et al. (2011), Jardine et al. (2013a, b) and others employed calibration chambers in earlier displacement pile studies. The Purdue University 'half-chamber' experiments provided comprehensive DIC measurements of the deformations and strains developed during monotonic installation. Half-circular cone tipped 31.75 mm diameter, relatively smooth brass piles penetrated pressurized sand masses retained in a half-cylindrical 1680 mm diameter, 1200 mm high steel chamber. One pile was installed for each fresh sand mass and DIC data were measured through a smooth vertical glass wall whose friction was assumed to have no effect on the sand strains. The average surface roughness R_a of the pile shaft and cone were ≈ 0.8 μm, both may have increased over time through the multiple tests undertaken. Arshad's DIC analysis considered incremental displacement fields, with 0.415 mm steps in pile penetration between consecutive frames, allowing the full displacement paths and post-penetration accumulated displacement fields to be calculated. The variations in the resulting Green-Lagrange strain tensor field were quantified by applying the post-processing VIC-2D software tool to multiple soil sub-elements (Arshad 2014).

Three silica sands with different crushability were tested after deposition at varying initial densities. A range of vertical surcharge pressures were applied by pressured membranes at the top of the chamber. This paper concentrates on the experiments conducted on dense (D_r = 82%) #2Q-ROK sand masses under a 50 kPa surcharge pressure for which the experimental cone tip resistance profile increases sharply with depth and tends to a quasi-stable q_c = 10–11 MPa when tip depth z > 300 mm, as shown in Fig. 1.

Test sand and model parameters

The #2Q-ROK test sand is a coarse-grained, silica sand mined from Oriskany quarzitic sandstone at Berkeley Spring in West Virginia. It has angular particles and the index properties summarized in Table 1. The Authors undertook suites of drained triaxial tests on #2Q-ROK that enabled a similar calibration process to that conducted in their earlier studies with Fontainebleau NE34 sand. An advanced electromechanical triaxial testing system described by Yang and Pan (2017) was employed in this study. Triaxial specimens of 70 mm in diameter and 140 mm in height were prepared using the air pluviation method. Specimens with initial relative densities between 80–82% were tested to assess how shearing resistance and dilatancy angles varied with strain and confining pressures ranging from 100 to 1000 kPa. The drained triaxial compression tests ran to axial strains exceeding 30%, giving the peak dilatancy and shearing resistance angles listed in Table 2. Critical state relationships were also established in both p'-q (Fig. 2a) and e-$(p')^{0.7}$ (Fig. 2b) planes. The final p'-q states could be fitted by a single M value which, under triaxial compression, is related to the critical angle of shearing resistance by:

$$M = \frac{q_{cs}}{p'_{cs}} = \frac{6 \sin \varphi'_{cs}}{3 - \sin \varphi'_{cs}} \quad (1)$$

The critical state φ' = 32.1°, close to 32.3° reported from direct shear tests by Arshad (2014). Fig. 2(b) shows how the critical state e–p' trend could be fitted by a power law with exponent = 0.7, after Li and Wang (1998).

The measured shear resistance and dilatancy angles can be considered within the state parameter framework of Been and Jefferies (1985), in which the state parameter $\xi = e - e_c$ is defined by the difference between the current void ratio e and critical void ratio e_c corresponding to the current mean stress p'. Figs. 3(a) and (b) indicate how the experimental dilatancy angle ψ' and shearing resistance angle φ' correlate with ξ, with following approximately linear and quadratic

trends respectively that can be fitted with reasonable accuracy by $\psi' = 928.69\ \xi^2 - 106.63\ \xi$ and $\varphi' = -54.75\ \xi + 32.21$.

It is also important for simulations to match the sand's stiffness, which is likely to be highly non-linear as well as pressure and density dependent: Seed and Idriss (1970), Hardin et al. (1972), Kuwano and Jardine (2003) or Jardine (2014). Resonant column tests were conducted by the authors on #2Q-ROK sand in an Energy Injecting Virtual Mass (EIVM) resonant column system (Yang et al. 2019) to obtain stiffness-strain curves for D_r = 82%, considering effective confining pressures from 50–500 kPa. The specimens were prepared using the air pluviation method and had 38 mm in diameter and 81 mm in height. The maximum shear moduli varied with pressure as depicted in Fig. 4(a), with extrapolation being made for the shear moduli developed under any higher pressures. Two curves illustrating how operational stiffness varied with shear strain and stress level are presented in Fig. 4(b), covering both a high- and low-pressure cases. Pre-yield behavior was otherwise treated as being non-linear (isotropic) elastic with a Poisson's ratio of 0.25, which was adopted according to experimental evidence summarized by Wichtmann and Triantafyllidis (2010), who found that the Poisson's ratio of a quartz sand increases with increasing coefficient of uniformity C_u and provided the range being 0.26–0.33 for C_u = 1.5 (C_u = 1.43 for #2Q-ROK). It is recognized however, that this treatment simplifies the true stiffness behavior of sands (as explored for example by Kuwano and Jardine 2002) to a considerable degree.

Modelling and constitutive parameter calibration

The half-pile calibration chamber installation was modelled with axisymmetric meshes applying the ALE option within ABAQUS. The dimension and boundary conditions of the model are shown in Fig. 5. The finite element type is CAX4R (four-node axisymmetric element with reduced

integration). The solid brass pile was treated as a rigid Lagrangian body with the correct cone tip ($D = 2R = 31.75$ mm), a total length of 0.915 m and a 0.6 m final embedment (L_p), giving ($L_p/R \approx 38$). The sand mass was regarded as deformable material subject to ALE adaptive mesh control. The same dimensions as the calibration chamber were adopted, with radial (half diameter) width w = 0.84 m, height H = 1.2 m, $w/R \approx 53$, which is sufficient to minimize boundary effects (Ghionna and Jamiolkowski 1991; Salgado et al. 1998). The pile-soil interface was modelled as surface-to-surface contact, in which the pile is treated as master surface and sand as the slave. The penalty friction formulation was adopted with a friction coefficient of 0.396 (or $\delta' = 21.6^o$) found in interface shear tests by Arshad (2014) employing the same brass and surface roughness. This coefficient fits the bilinear relationship with normalized roughness (R_n/D_{50}) proposed by Uesugi and Kishida (1987). The smooth brass pile would not have invoked the markedly dilative interface radial stress changes and notably higher shaft friction angles observed by Lehane et al. (1992) and Jardine et al. (2013) in instrumented field and laboratory pile tests that employed comparable roughness to industrial piles.

A variable parameter, Mohr-Coulomb model was employed to represent the sand. Simple Mohr-Coulomb models have been extensively applied in large-deformation simulations (see for example Yimsiri et al. 2004; El Kortbawi et al. 2022), and an elaborated (state and strain level) dependent variant was preferred in the study owing to its relatively stable performance and its lower susceptibility to ALE variable mapping induced errors after re-meshing than more complex constitutive models. The parameters were calibrated to the Authors' triaxial and resonant column tests, with the shearing resistances, dilatancy angles and stiffnesses varying very significantly and realistically with both the local invariant shear strain level and sand state (mean effective stress

and void ratio). Non-linear stiffness, which was not considered by Yang et al. (2020), was addressed in the present study to better match the experimental displacement fields. The model deployed, which was suitable for monotonic pile penetration, is not able to capture any impact of load cycling during installation. Nor could it capture the effects of any grain crushing.

The first ALE analyses aimed to simulate the experimental CPT q_c profile. Vertical pressure was gradually built up to 50 kPa over the upper sand surface of the sand mass, assuming a lateral stress coefficient at rest (before any pile installation) of $K_0 = 1 - \sin\varphi' = 0.47$ which is considered suitable for cohesionless quartz sands, before advancing the pile at a constant velocity into the 'chamber'. Convergence studies checked the solutions' sensitivity to mesh geometry and penetration rate and found the most computational efficient way of obtaining well-defined, stable cone resistance q_c profiles, as described in the supplementary material. A mesh with a size of 0.004 m and a velocity of 0.01 m/s were used in this study. Minor changes were applied to input model parameters to optimize the degree of fit with experiments, employing sand mass partitioning as described by Yang et al. (2020). The final operational Mohr-Coulomb model parameter set is listed in Table 3, and the details of the continuously updated partitions of sand domain throughout the penetration were defined in the supplementary material. Fig. 1 compares the resulting q_c trace with Arshad's experiment.

Analytical results for soil displacements and comparison with experiments

Displacement pattern around pile tip during penetration

The ALE analyses led directly to predictions for the displacement patterns developed around the advancing pile tip. Fig. 6 illustrates the incremental displacement vectors at varying normalized depths z/R = 6 and 20, comparing the numerical and experimental results. The incremental

displacement fields were evaluated over the 2.059 mm (or 0.13*R*) penetration steps applied in Arshad's DIC image analysis process. No discernible upward flow of the soil mass was predicted after penetrations exceeded *z*/*R* = 6, as noted in the experiments. The maximum predicted incremental soil displacement, amounting to ≈ 0.1*R*, occurs on the cone surface at a 0.5*R* radial distance from the pile axis. The displacement vectors remain vertical below the tip and rotate radially outward further away from the pile axis. The average degree of rotation θ_{ave} was quantified, as suggested by Arshad et al. (2014) by evaluating Eqs. (2) to (4) within the volume of revolution contained within the box defined in Fig. 6, which is bounded by (i) the cone surface, (ii) the vertical boundaries *h* = 0 and -4.5*R* and (iii) the radial sides of cylinders with radii *r* = 0 and 5*R*.

$$\theta_{ave} = \frac{\sum_{i=1}^{n_{el}} \theta_i l_i 2\pi r_i dr}{\sum_{i=1}^{n_{el}} l_i 2\pi r_i dr} \tag{2}$$

where

$$\theta_i = \tan^{-1}\left(\frac{v_i}{u_i}\right) \tag{3}$$

$$l_i = \sqrt{{u_i}^2 + {v_i}^2} \tag{4}$$

and u_i and v_i are the radial and vertical components of displacement of each soil element *i* in the subdomain, respectively; l_i and θ_i are the magnitude and the direction of the displacement vector of soil element *i* with respect to the horizontal direction, respectively; n_{el} is the total number of soil elements in the subdomain; r_i is the radial distance between the center of element *i* and the cone axis; *dr* is the element width – which can only be eliminated from Eq. (2) if all the elements have the same width.

The simulated θ_{ave} angles increase as the tip vertical stresses grow with penetration depth *z*/*R* in Fig. 6, as observed experimentally by Arshad et al. (2014). However, the simulated angles exceed

319 the experimental results significantly, by ≈ 10°. Yang et al. (2010) noted that grain crushing was
320 important beneath cone tips once q_c exceeded around 5 MPa in less angular NE34 test sand.
321 Although grain crushing and shear band formation is not captured in the present analyses, Arshad
322 et al. (2014) noted that both were significant with #2Q-ROK sand and reduced the average degree
323 of vector rotations that developed away from the pile axis. It is likely that the analytical
324 discrepancies would be reduced if the 'gross' yielding of the sand (under elevated spherical stresses)
325 and grain crushing had been captured under the pile tip.

326 Further insight is given in Fig. 7 regarding the incremental displacement vectors developed
327 along the three prescribed paths emanating from the origins indicated in Fig. 7a. The normalized
328 displacement vector lengths (l/R) and orientations (θ) are plotted against normalized distance d/R
329 from the respective path origins in Figs. 7b, 7c, and 7d, considering stages when the pile tip reached
330 normalized depths z/R of 6 and 20. The displacement magnitudes diminish markedly with distance
331 along each path. The maximum incremental displacements develop along the intermediate Path 2
332 and the (far smaller) minima along horizontal Path 3. Noting that the vectors developed under the
333 pile axis must remain axial, the Path 1 vectors, plotted along a path set at a radial distance of $0.3R$
334 (see Fig. 7a) from the axis remain near vertical, while the Path 2 and 3 vectors rotate towards the
335 horizontal as their distance increase. The six displacement trend curves are plotted together in Fig.
336 7e. While all follow similar trends, their lengths remain unequal until $d/R > 6$ and so vary from a
337 precisely hemi-spherical cavity expansion pattern.
338
339 ***Displacement zones around the tip***

340 The distribution of displacement vector directions depends on sand density, crushability,
341 surcharge level and pile shaft roughness. Following Arshad et al. (2014) it is convenient to partition

342 the deforming zones of sand into the simplified scheme depicted in Fig. 8(a). Zone I is a region
343 where axial compression dominates with the ratio of the vertical to radial increments $\Delta v/\Delta u > 2$.
344 The ratio applying in the third 'cavity expansion' has the reverse ratio with $\Delta u/\Delta v > 1$ and $1 > \Delta u/\Delta v >$
345 0.5 in the second 'transition' zone.

346 To better understand the displacement paths imposed by cone penetration, Figs. 8(b) to 8(g)
347 consider the $\Delta u/R$ and $\Delta v/R$ ratios applying at the key elements (E_1, E_2, E_3, E_4, E_5 and E_6) designated
348 in Arshad's analysis after applying a relatively large incremental pile tip penetration of 1R to a pile
349 whose tip had already reached 20R, presenting both predictions and experimental findings. E_1 is
350 located near to the cone tip (r = 0.2R, z = 20.32R) and experiences a vertical displacement
351 increment Δv ~0.5R which is around 20% lower smaller than measured experimentally, albeit over
352 the shorter 'gauge length' imposed by the DIC technique's difficulty in tracking particles in the
353 crushing zone and shear band formed around the shaft. Note that element E_1 is shifted radially
354 from the axis by 0.2R. The experimental counterpart appears to show less radial movement,
355 although its exact position was not specified by Arshad et al. (2014). Addressing the yielding of the
356 sand under the elevated stresses and the grain crushing process should bring the predictions closer
357 to the measurements. However, any friction between sand and the glass DIC observation plane
358 would also tend to artificially reduce the experimental soil strain.

359 The transition zone elements E_2, E_3, E_4, retain the $\Delta v/\Delta u > 1$ pattern, but with the numerical
360 predictions for vertical movements now exceeding the measurements. The radial movement
361 predictions tend to fall around, or below the experimental trends. The trends for E_5 and E_6 shift to
362 give $\Delta v/\Delta u < 1$ and the numerical predictions exceed the predictions quite significantly, especially
363 for the vertical components.

Displacement paths followed behind the advancing pile tip

Arshad et al. (2014) also reported the displacement paths followed by soil elements *A* to *H*, set initially at 294 mm below ground surface and at r/R = 0.5, 1, 1.5, 2, 3, 4, 6, and 8, as shown in Fig. 9. This depth (equivalent to ≈ 18.5*R*), at the top of the region showing q_c values that were quasi-constant with depth. Fig. 9 illustrates the displacement paths measured experimentally after penetration to ≈ 30*R*, and the equivalent numerical predictions. The intense concentration of movement in the near field around the shaft is evident, as is the generally good agreement between the numerical and experimental trends. Interestingly, inward radial displacement is both predicted and observed over the final stages of penetration. Such unloading strain paths are crucial to explaining the dramatic reductions in local shaft radial stresses that take place behind the pile tip with increasing h/R (Jardine et al. 2013a, b).

The evolution of normalized radial (u/R) and vertical (v/R) displacements of Elements *B*–*E* is explored further in Fig. 10 covering tip positions from ground surface to full depths ≈ 25*R* in the experiments and 30R in the analysis. As noted above, the elements were located at r/R = 1, 1.5, 2, 3 from the axis prior to pile installation. Four stages are identified which reflect the points moving into the different deformation zones defined by Arshad et al. (2014) as the tip approaches from above and passes below the level of the four Elements. Stage 1 signifies the start of axial compression; stage 2 the onset of radial cavity expansion and stage 3 its end. Finally state 4 indicates the end of motion. It is clear the sand mass senses the pile tip's approach from above long before it reaches each Elements' level, where the vertical and radial displacements increase abruptly. It is also evident that both Elements *B* and *C* undergo greater vertical than radial displacements throughout installation, with generally good agreement between predictions and

387 measurements. Element *B* is displaced radially significantly (stage 2) until the cone tip passes the
388 element level after which the measured movements reversed between stages 3 and 4, but to a
389 lesser degree than predicted. This feature may result from the simplified elastic pre-yield behavior
390 assumed for modelling failing to reproduce hysteresis in the test sand. The peak radial
391 displacement occurs when the tip was positioned 1.5*R* below the four Elements' initial level.

392 The other Elements show similar trends with tip depth and the numerical results remain in
393 broad agreement with Arshad et al.'s experiments. Unlike the radial displacement trends, the
394 vertical displacements generally increase monotonically and only Element *E* shows a slight upward
395 rebound after the pile tip passes; it also shows a relatively wide divergence between the
396 experimental and numerical trends.

397 The radial and vertical components of displacement developed beneath the cone tip during
398 monotonic penetration are examined further in Fig. 11 considering again Elements set at z ≈ 20*R*
399 and located at *r*/*R* = 1, 1.5, 2, 3, 5 and 8, but plotting displacements against relative pile tip depth
400 *h*/*R*. The plots confirm the patterns of strains starting to grow dramatically as the pile tip
401 approaches within ≈ 3 radii of the Element level (i.e., *h*/*R* = -3), peaking as the cone shoulder passes
402 the Element level (*h*/*R* = 0) and then reducing with increasing (positive) *h*/*R*. The predicted vertical
403 and radial components show comparable trends to the experiments, although the latter tend to
404 show more marked post-peak reductions with *h*/*R*.

405

406 ***Final, post-installation, displacement field***

407 The displacement fields predicted after penetration to 20*R* are illustrated as normalized radial
408 and vertical component contours in Fig. 12(a) and (c) respectively, which match well the
409 experiments of Arshad et al. (2014) shown as Fig. 12(b) and (d). The radial contours appear nearly

parallel with the pile axis at points above the pile tip shoulder, while the vertical movements diminish markedly with increasing h/R. The parallel radial displacement contours follow an approximately cylindrical cavity expansion deformation pattern above the pile tip shoulder, whereas the rapidly diminishing vertical displacements provide another reflection of the important 'h/R effect' emphasized by Jardine et al (2013a, b) and Yang et al (2020).

Analytical results for soil strains and comparison with experiments

The radial E_{rr}, vertical E_{zz} and shear strain E_{rz} were calculated throughout each stage of the pile penetration analysis, taking normal strains as positive in compression. Fig. 13 illustrates the spatial distribution of radial, vertical and shear strain increments found around the conical tip after incremental penetrations of $0.13R$ applied after tip penetration to $z = 20R$. Noting that the experimental strain fields are harder to resolve accurately than the displacements from which they are derived, comparisons are made with Arshad's experiments.

E_{rr} strains

Figs. 13(a) and (b) illustrate the radial (E_{rr}) straining patterns, with increments developing over the $0.13R$ pile tip displacement step, forming a tensile bulb that extends to about $3R$ below the pile tip. The strains become compressive a short distance above the tip and the simulations indicate larger maxima (≈ 5%) and a larger area of significant straining than the experiments (≈ 3%), possibly due to unmodeled grain crushing and shear banding, as noted earlier.

E_{zz} strains

The equivalent vertical (E_{zz}) strain increment patterns are illustrated in Figs. 13(c) and (d). The numerical simulations and experiments show broadly similar patterns beneath the tip, although the analyses again predict larger maxima than the experiments due to grain crushing and shear

435 banding. Compressive vertical straining dominates below the conical tip and part-way up the
436 conical tip face, confirming that the stress state within soil elements beneath the tip is similar to
437 that under triaxial compression. However, this pattern changes markedly with distance above the
438 tip and vertical straining reduces sufficiently to become negative at points near the conical tip's
439 shoulder.

440 Grain crushing is also known to affect the strain fields; Yang et al., (2010). Experiments by
441 Arshad (2014) confirmed that the vertical and volume strains beneath the pile tip were larger in
442 tests involving the less crushable ASTM20-30 sand than with the crushable #2Q-ROK material
443 considered in this study.

444

445 ***E_{rz} shear strains***

446 The equivalent shear strain (E_{rz}) contours shown in Figs. 13(e) and (f) indicate a single 'bulb'
447 covering the transition zone highlighted by Salgado and Prezzi (2007). The numerical patterns agree
448 well with those reported by Arshad (2014) although showing larger maxima (≈ 7%) than the
449 experiments (≈ 5%).

450

451 ***Final, post-installation, strain fields***

452 Summaries of the total (cumulative) radial (E_{rr}), vertical (E_{zz}) and shear (E_{rz}) strains developed
453 after penetration to L_p = 20R are shown in Fig. 14, presenting both the simulations and
454 experimental data. Naturally, the total strains exceed the incremental changes considered in Fig.
455 13. The predicted and measured radial strains show similar distributions beneath and around the
456 pile tip, but differ more significantly higher on the shaft, where E_{rr} appears to be over-predicted
457 and the experiments indicate more marked radial contraction around the shaft. Similar features
458 can be observed in the E_{zz} and E_{rz} contours, with the strains appearing over-predicted along much

459 of the pile shaft. These differences are interpreted as reflecting the development of a
460 discontinuous shear zone of fractured and densified sand around the pile shafts, where the
461 operational interface friction angles fall well below critical state φ', as observed experimentally by
462 Yang et al. (2010).
463
464 ***Predictions for pile loads and stress regime generated around pile shaft***
465 The numerical analyses provide full sets of predictions for the pile loads during penetration
466 and variations with r/R of the shaft stress components at various h/R, r/R positions. The first point
467 to note from Fig. 1 is that the good agreement was assured between measured and predicted tip
468 bearing pressures as part of the calibration procedure. Converting Arshad's experimental half-pile
469 shaft load to the full pile case indicates a total load of 9.15 kN after penetration to z = 37.8R (600
470 mm) which is comparable to, but 22% lower than, the predicted 11.67 kN.
471 Given the low roughness of Arshad's brass pile, the stress regime predicted on the shaft and
472 within the sand mass may be expected to fall closer to the 'stationary' patterns observed in
473 comparable calibration chamber experiments on relatively rough Mini-ICP piles than those
474 observed while the pile is 'moving'. Far greater differences can be expected near the pile tip, where
475 moving pile conditions impose very high pile tip stresses. Jardine et al. (2013a) discuss the extreme
476 difficulty of making local stress measurements reliably, given the highly nonuniform stress
477 conditions developed around small diameter piles and the potential disturbance of the sand's state
478 caused by the presence of the stress sensors. Fig. 15 presents the numerical predictions for the
479 radial σ_r, circumferential σ_θ, and vertical stresses σ_z stresses applying at three vertical levels above
480 the pile tip at the end of penetration, covering the $5 < h/R < 15$ range, normalized by the predicted
481 local CPT resistances indicated in Fig. 1. The profiles all show pronounced maxima within the 2 <

482 $r/R < 5$ radial distance range which agree broadly with the steeply non-uniform experimental trends
483 reported by Jardine et al. (2013a) and earlier numerical modelling by Yang et al. (2020). The radial
484 stresses developed on the shaft all reduce markedly with elevation above the pile tip, contributing
485 to the "h/R effect" identified in the field by Lehane et al. (1992). While this field feature has also
486 been referred to as "friction fatigue" by White and Lehane (2004), the predicted variations are
487 purely products of the pile geometry; repetitive loading by hammer blows during field pile driving
488 may further accentuate the reduction of stresses with growing h/R. The equivalent σ_θ distributions
489 shown in Fig. 15b indicate $\partial\sigma_\theta/\partial(r/R)$ gradients that are steeper than those for $\partial\sigma_r/\partial(r/R)$ and lead
490 to σ_θ exceeding σ_r close to the shaft (at $r/R = 1$) by degrees that increase with h/R. Fig. 15c illustrates
491 the vertical stresses obtained above the tip, showing lower values than the other components and
492 a trend towards a far-field value comparable to the 0.5%q_c vertical pressure applied at the top of
493 the calibration chamber.

494 It is also interesting to compare the predicted and measured axial loads and shaft stresses
495 with the outcomes of CPT based design procedures, while recognizing that the latter aim to match
496 field load-test conditions at stages some days or weeks after driving which generally exceed those
497 available at the end of driving by perhaps 50% (Jardine et al. 2006). The total axial capacity Q_t
498 measured under compression loading is the sum of the shaft Q_s and base Q_b capacities

499 $$Q_t = Q_s + Q_b = \pi D \int_0^{z_{tip}} \tau_f dz + q_b A_b \quad (5)$$

500 where D = pile diameter; τ_f = local ultimate shaft friction; z = depth; q_b = end bearing resistance;
501 and A_b = base area. In the ICP-05 procedure, q_b is expressed as:

502 $$q_b/q_{c,avg} = \max[1 - 0.5 \log\left(\frac{D}{D_{CPT}}\right),\ 0.3] \quad (6)$$

503 This expression indicates that q_b is practically equivalent to q_c for the current model pile case,

as has been assumed in this paper. The local ultimate shaft friction τ_f in Eq. (5) is:

$$\tau_f = (\sigma'_{rc} + \Delta\sigma'_{rd})\tan\delta_f \quad (7)$$

where $$\sigma'_{rc} = \left[0.029 q_c \left(\frac{\sigma'_{v0}}{p_a}\right)^{0.13} \max\left(\frac{h}{R}, 8\right)^{-0.38}\right] \quad (8)$$

and $$\Delta\sigma'_{rd} = 2\Delta r\, G/R \quad (9)$$

in which σ'_{v0} = free-field vertical effective stress; p_a = the atmospheric pressure; δ_f = the interface failure angle; σ'_{rc} is the stationary radial effective stress acting on the shaft and $\Delta\sigma'_{rd}$ is the dilatant increase in local radial stress during pile loading, which is related to Δr = twice the pile surface's center-line average roughness. Jardine et al. (2005) give an expression for estimating G, the sand's shear modulus, from local CPT resistance.

Profiles with depth are plotted in Fig. 16 of the radial stress components evaluated from Eqs. 8 and 9 for the full penetration to z = 37.8R (600 mm) case, along with the numerical predictions, normalized by the local CPT resistance q_c as averaged 1.5 diameters above and below the tip. The numerical predictions fall relatively close to the ICP-05 and UWA-05 predictions over most of the shaft length. The analysis indicates higher stresses than the ICP at low h/R, primarily due to the high tip loads applied by the moving pile, which do not apply to the stationary, pre-loading, σ'_{rc} conditions considered in the ICP.

Taken with the measured δ_f angle and roughness of pile shaft, the ICP-05 expressions predict a medium-term (10 to 30 day) age shaft capacity of 2.35 kN for this case, while the measured value (adjusted to a full pile) at installation was 1.24 kN. The ICP-05 base resistance is (by design) close to that measured. The alternative UWA-05 (Lehane et al. 2005) treatment indicates a slightly higher shaft resistance of 2.84 kN and a base resistance ≈ 40% below that measured. However, it is important to recall that the above design procedures aim to match field conditions around

526 dynamically driven, rough-surfaced, field piles at 10-to-30 day ages. The smooth brass model pile's
527 anomalously low shaft resistance might reflect its monotonically jacked installation, lack of ageing
528 or the calibration chamber boundary conditions. Field tests on mild steel micro-piles driven in
529 sands show sharp capacity growth with time after driving (Carroll et al. 2020).
530
531 **Summary and conclusions**
532
533 Numerical analyses presented in this paper consider the deformations generated by
534 displacement pile installation in sand calibration chamber experiments. ALE finite element
535 solutions were obtained with a variable parameter Mohr-Coulomb model calibrated to new triaxial
536 and resonant column experiments undertaken by the Authors to match the displacement and
537 strain fields observed by Arshad et al. (2014) in model tests employing advanced DIC techniques.
538 The pile tip and shaft loads have also been considered and stress solutions have been reported
539 that add insights into calibration chamber test outcomes. The study leads to the following main
540 conclusions:
541
542 1. A relatively simple Mohr-Coulomb model with state-dependent dilation and shearing
543 resistance angles and Young's moduli was able to capture most features of the sand's
544 behavior during pile installation.
545 2. The numerically predicted displacements and strains showed good qualitative agreement
546 with the complex patterns established experimentally.
547 3. Interesting points of divergence were also found. The soil strains were over-predicted by
548 significant margins in some cases due to grain crushing and shear band formation processes
549 that were not addressed in the ALE modelling but were demonstrated in the Purdue
550 University's experiments by considering sands with different grain crushability.

4. The complex stress distributions predicted within the sand mass showed good qualitative agreement with measurements made in other programs of calibration chamber tests and predictions made with ICP-05 and UWA-05 design methods.

Further research is required to investigate (i) how grain crushing, shear banding, and interface modelling, as well as repetitive (cyclic) loading applied during field pile driving affect the stress and strain conditions imposed by installation and (ii) how the stress regime developed around the pile may change over time as piles age in-situ.

Data Availability Statement

All data, models, and code that support the findings of this study are available from the corresponding author upon reasonable request.

Acknowledgements

This research was supported by Natural Science Foundation of China (51761130078) and Advanced Newton Fellowship (NA160438) that were jointly awarded by Royal Society of the UK and NSFC, and Major International Joint Research Project of NSFC (52020105003). Gratitude is also extended to Professor Rodrigo Salgado and his former student Dr. Mazhar Arshad, for their patience in answering many questions regarding their DIC experiments.

References

Andò, E., Hall, S. A., Viggiani, G., Desrues, J., and Bésuelle, P. 2012. “Grain-scale experimental investigation of localised deformation in sand: a discrete particle tracking approach.” *Acta Geotech*. 7(1), 1-13.

574 API (American Petroleum Institute). 2014. *ANSI/API recommended practice 2GEO*. 1st Ed., RP2GEO.
575 Washington, DC: API.
576 Arroyo, M., Butlanska, J., Gens, A., Calvetti, F., and Jamiolkowski, M. 2011. "Cone penetration tests
577 in a virtual calibration chamber." *Géotechnique* 61(6), 525-531.
578 Arshad, M.I. 2014. "Experimental study of the displacements caused by cone penetration in sand."
579 Ph.D. thesis, Purdue University.
580 Arshad, M.I., Tehrani, F.S., Prezzi, M., and Salgado, R. 2014. "Experimental study of cone
581 penetration in silica sand using digital image correlation." *Géotechnique* 64(7), 551-569.
582 Bardenhagen, S.G , Brackbill, J.U, and Sulsky, D. 2000. “The material-point method for granular
583 materials.” *Comput. Methods Appl. Mech. Eng*. 187(3/4):529-541.
584 Bardenhagen, S.G., Guilkey, J.E., Roessig, K.M., Brackbill, J.U., Witzel, W.M., and Foster, J.C. 2001.
585 “An improved contact algorithm for the material point method and application to stress
586 propagation in granular materials.” *Comput. Model Eng. Sci*. 2(4), 509–522
587 Been, K., and Jefferies, M.G. 1985. "A state parameter for sands." *Géotechnique* 35(2), 99-112.
588 Butlanska, J., Arroyo, M., Gens, A., and O’Sullivan, C. 2014. "Multi-scale analysis of cone
589 penetration test (CPT) in a virtual calibration chamber." *Can. Geotech. J*. 51(1), 51-66.
590 Carroll, R., Carotenuto, P., Dano, C., Salama, I., Silva, M., Gavin, K. and Jardine, R.J. 2020. "Field
591 experiments at three sites to investigate the effects of age on steel piles driven in sand."
592 *Geotechnique* 70 (6), 469-489.
593 Ceccato, F., Beuth, L., Vermeer, P.A., and Simoninia, P. 2016. “Two-phase material point method
594 applied to the study of cone penetration”. *Comput. Geotech*. 80: 440-452.
595 Chow, F.C. 1997. "Investigations into displacement pile behaviour for offshore foundations." Ph.D.

thesis, Imperial College, London.

Ciantia, M., O'Sullivan, C., and Jardine, R.J. 2019. "Pile penetration in crushable soils: Insights from micromechanical modelling." *17th European Conference on soil Mechanics and Geotechnical Engineering (ECSMGE 2019)*. 1-20.

Coombs, W. M., Charlton, T. J., Cortis, M., and Augarde, C. E. 2018. Overcoming volumetric locking in material point methods. *Comput Methods Appl Mech Eng*, 333, 1-21.

Dassault Systèmes Simulia. 2016. *Abaqus 2016 analysis user's manual*. Providence, RI: Simulia.

Doreau-Malioche, J., Combe, G., Viggiani G., and Toni, J.B. 2018. "Shaft friction changes for cyclically loaded displacement piles: an X-ray investigation." *Géotechnique Lett*. 2018, 8(1): 66-72.

El Kortbawi, M., Moug, D. M., Ziotopoulou, K., DeJong, J. T., and Boulanger, R. W. 2022. " Axisymmetric Simulations of Cone Penetration in Biocemented Sands." *J. Geotech. Geoenviron. Eng*. 148(11), 1090-0241.

Foray, P., Balachowski, L., and Colliat, J. L. 1998. "Bearing capacity of model piles driven into dense over-consolidated sands." *Can. Geotech. J*. 35(2), 374-385.

Foray, P., Colliat, J.L., and Nauroy, J.F. 1993. "Bearing capacity of driven model piles in dense sands from calibration chamber tests." In *Proc., 25th Offshore Technology Conf.,* Houston: Offshore Technology Conference.

Gao, L., Guo, N., Yang, Z.X., and Jardine, R.J. 2022. "MPM modeling of pile installation in sand: Contact improvement and quantitative analysis." *Comput. Geotech.* 151, 104943.

Gavin, K.G., and Lehane, B.M. 2003. "The shaft capacity of pipe piles in sand." *Can. Geotech. J.* 40(1), 36-45.

618 Ghionna, V.N., and Jamiolkowski, M. 1991. “A critical appraisal of calibration chamber testing of
619 sands.” In *Proceedings of the 1st International Conference on Calibration Chamber Testing*,
620 Clarkson Univ. Potsdam, USA, 13-37.
621 Hardin, B.O., and Drnevich, V.P. 1972. “Shear Modulus and Damping in Soil: Design Equations and
622 Curves.” *Journal of the Soil Mechanics and Foundations Division*. 98(7), 667-692.
623 Henke, S. 2008. "Herstellungseinflüsse aus Pfahlrammung im Kaimauerbau." Ph.D. thesis,
624 Veröfentlichungen des Instituts für Geotechnikund Baubetrieb der TU.
625 Henke, S. 2010. "Influence of pile installation on adjacent structures." *Int. J. Numer. Anal. Methods*
626 *Geomech.* 34(11), 1191-1210.
627 Henke, S., Qiu, G., and Grabe, J. 2010. "A Coupled Eulerian-Lagrangian approach to solve
628 geotechnical problems involving large deformations." In *Proc., 7th European Conf on*
629 *Numerical Methods in Geotechnical Engineering (NUMGE)*, 233-238.
630 Iskander, M.G., Sadek, S., and Liu, J. 2002. “Optical measurement of deformation using transparent
631 silica gel to model sand.” *Int. J. Phys. Model. Geotech.* 2(4), 13-26.
632 Jardine, R.J., Chow, F.C., Overy, R., and Standing, J.R. 2005. *ICP design methods for driven piles in*
633 *sands and clays*. London: Thomas Telford.
634 Jardine, R.J., Standing, J.R., and Chow, F.C. 2006. "Some observations of the effects of time on the
635 capacity of piles driven in sand." *Géotechnique* 56(4), 227-244.
636 Jardine, R.J., Zhu, B.T., Foray, P., and Yang, Z.X. 2013a. "Measurement of stresses around closed-
637 ended displacement piles in sand." *Géotechnique* 63(1), 1-17.
638 Jardine, R.J., Zhu, B.T., Foray, P., and Yang, Z.X. 2013b. "Interpretation of stress measurements made
639 around closed-ended displacement piles in sand." *Géotechnique* 63(8), 613-627.

640 Jardine, R.J. 2014. “Advanced laboratory testing in research and practice: the 2nd Bishop Lecture.”
641 *Geotechnical Research*, 1(1): 2-31.
642 Jardine, R.J., and Yang, Z.X. 2018. “Joint research into the behaviour of driven piles.” In *Proceedings*
643 *of China-Europe Conference on Geotechnical Engineering*, *SSGG*, edited by W. Wu and H.-S. Yu,
644 961-972.
645 Jardine, R.J. 2020. “Geotechnics, energy and climate change: the 56th Rankine Lecture.”
646 *Géotechnique* 70(1): 3-59.
647 Kishida, H., and Uesugi, M. 1987. “Tests of the interface between sand and steel in the simple shear
648 apparatus.” *Géotechnique* 37(1), 45–52.
649 Ko, J., Jeong, S., and Lee, J.K. 2016. "Large deformation FE analysis of driven steel pipe piles with
650 soil plugging." *Comput. Geotech*. 71, 82-97.
651 Kobayashi, T., and Fukagawa, R. 2003. “Characterization of deformation process of CPT using X-ray
652 TV imaging technique.” In *Third International Conference on Deformation Characteristics of*
653 *Geomaterials*. 43-47.
654 Kuwano, R., and Jardine, R.J. 2007. “A triaxial investigation of kinematic yielding in sand.”
655 *Géotechnique* 57(7): 563-579.
656 Lehane, B.M., Jardine, R.J., Bond, A.J., and Frank, R. 1993. "Mechanisms of shaft friction in sand
657 from instrumented pile tests." *J. Geotech. Eng*. 119(1), 19-35.
658 Lehane, B.M., and Gill, D.R. 2004. “Displacement fields induced by penetrometer installation in an
659 artificial soil.” *Int. J. Phys. Model. Geotech*. 4(1), 25-36.
660 Lehane, B.M., Lim, J. K., Carotenuto, P., Nadim, F., Lacasse, S., Jardine, R.J., and van Dijk, B.F.J. 2017.
661 "Characteristics of unified databases for driven piles." In *Proc., 8th International Conference,*

662 *Offshore Site Investigation and Geotechnics: Smart solutions for future offshore developments*.
663 162-191.
664 Lemiale, V., Nairn, J., and Hurmane, A. 2010. “Material point method simulation of equal channel
665 angular pressing involving large plastic strain and contact through sharp corners.” *Comput.*
666 *Model Eng. Sci*. 70(1), 41–66.
667 Liu, W. 2010. “Axisymmetric centrifuge modelling of deep penetration in sand.” Ph.D. thesis,
668 University of Nottingham.
669 Liu, J. 2003. “Visualization of three-dimensional deformations using transparent soil models.” Ph.D.
670 thesis, Polytechnic Institute of New York University.
671 Liu, S., and Wang, J. 2016. "Depth-independent cone penetration mechanism by a discrete element
672 method (DEM)-based stress normalization approach." *Can. Geotech. J*. 53(5), 871-883.
673 Lorenzo, R., da Cunha, R.P., Neto, M.P.C., and Nairn, J.A. 2018. "Numerical simulation of installation
674 of jacked piles in sand using material point method." *Can. Geotech. J*. 55(1), 131-146.
675 Mahutka, K. P., König, F., and Grabe, J. 2006. "Numerical modelling of pile jacking, driving and
676 vibratory driving." In *Proc., Int. Conf. on Numerical Simulation of Construction Processes in*
677 *Geotechnical Engineering for Urban Environment (NSC06)*. 235-246.
678 Mo, P.Q. 2014. “Centrifuge modelling and analytical solutions for the cone penetration test in
679 layered soils.” Ph.D. thesis, University of Nottingham.
680 Mo, P.Q., Marshall, A.M., and Yu, H.S. 2015 “Centrifuge modelling of cone penetration tests in
681 layered soils.” *Géotechnique* 65(6): 468-481.
682 Ni, Q.C.C.I., Hird, C.C., and Guymer, I. 2010. “Physical modelling of pile penetration in clay using
683 transparent soil and particle image velocimetry.” *Géotechnique* 60(2), 121.

Ngan-Tillard, D.J.M., Cheng. X.H., van Nes, J., and Zitha, P.L.J. 2005. “Application of x-ray computed tomography to cone penetration tests in sands.” In *GSP 138 Site Characterization and Modeling*, 1-12.

Otani, J., Mukunoki, T., and Sugawara, K. 2005. “Evaluation of particle crushing in soils using X-ray CT data.” *Soil Found*. 45(1), 99-108.

Paik, K., and Salgado, R. 2003. "Determination of bearing capacity of open-ended piles in sand." *J. Geotech. Geoenviron. Eng*. 129(1), 46-57.

Paik, K., Lee, J., and Kim, D. 2011. "Axial response and bearing capacity of tapered piles in sandy soil." *Geotech. Test. J*. 34(2), 122-130.

Paniagua, P., Andó, E., Silva, M., Emdal, A., Nordal, S., and Viggiani, G. 2013. “Soil deformation around a penetrating cone in silt.” *Géotechnique Lett*. 3(4), 185-191.

Phuong, N.T.V., van Tol, A.F., Elkadi, A.S.K., and Rohe, A. 2016. "Numerical investigation of pile installation effects in sand using material point method." *Comput. Geotech*. 73, 58-71.

Qiu, G., Henke, S., and Grabe, J. 2011. "Application of a Coupled Eulerian–Lagrangian approach on geomechanical problems involving large deformations." *Comput. Geotech*. 38(1), 30-39.

Rimoy, S., Silva, M., Jardine, R.J., Yang, Z.X., Zhu, B.T., and Tsuha, C.H.C. 2015. "Field and model investigations into the influence of age on axial capacity of displacement piles in silica sands." *Géotechnique* 65(7), 576-589.

Robinsky, E.I., and Morrison, C.F. 1964. "Sand displacement and compaction around model friction piles." *Can. Geotech. J*. 1(2), 81-93.

Salgado, R., Mitchell, J.K., and Jamiolkowski, M. 1998. "Calibration chamber size effects on penetration resistance in sand." *J. Geotech. Geoenviron. Eng.* 124(9), 878-888.

706 Seed, H.B., and Idriss, I.M. 1970. “Soil moduli and damping factors for dynamic response analysis.”
707 *Report No. UCB/EERC-70/10, Earthquake Engineering Research Center*, University of California,
708 Berkeley, December, 48 p.
709 Sheng, D., Eigenbrod, K.D., and Wriggers, P. 2004. "Finite element analysis of pile installation using
710 large-slip frictional contact." *Comput. Geotech*. 32(1), 17-26.
711 Sulsky, D., Chen, Z., and Schreyer, H.L. 1994. “A particle method for history-dependent materials.”
712 *Comput. Methods Appl. Mech. Eng*. 118(1-2): 179-196.
713 Taborda, D.M.G., Zdravković, L., Potts, D.M., Burd, H.J., Byrne, B.W., Gavin, K.G., Houlsby, G.T.,
714 Jardine, R.J., Liu, T., Martin, C.M., and McAdam, R.A. 2020. “Finite-element modelling of
715 laterally loaded piles in a dense marine sand at Dunkirk.” *Géotechnique* 70(11): 1014-1029.
716 Tehrani, F.S., Nguyen, P., Brinkgreve, R.B.J., and van Tol, A.F. 2016. "Comparison of press-replace
717 method and material point method for analysis of jacked piles." *Comput. Geotech*. 78, 38-53.
718 Tehrani, F.S., Arshad, M.I., Prezzi, M., and Salgado, R. 2018. "Physical modeling of cone penetration
719 in layered sand." *J. Geotech. Geoenviron. Eng*. 144(1), 04017101.
720 Tovar-Valencia, R.D., Galvis-Castro, A., Salgado, R., and Prezzi, M. 2018. "Effect of surface roughness
721 on the shaft resistance of displacement model piles in sand." *J. Geotech. Geoenviron. Eng*.
722 144(3), 04017120.
723 Tsuha, C.H.C., Foray, P.Y., Jardine, R.J., Yang, Z.X., Silva, M., and Rimoy, S. 2012. "Behaviour of
724 displacement piles in sand under cyclic axial loading." *Soil Found*. 52(3), 393-410.
725 Tran, Q. A., and Sołowski, W. 2019. Temporal and null-space filter for the material point method. *J.*
726 *Numer. Methods Eng*. 120(3), 328-360.
727 Wang, D., Bienen, B., Nazem, M., Tian, Y.H., Zheng, J.B., Pucker, T., and Randolph, M.F. 2015. "Large

728 deformation finite element analyses in geotechnical engineering." *Comput. Geotech*. 65, 104-
729 114.
730 Wang, J., and Zhao, B. 2014. "Discrete-continuum analysis of monotonic pile penetration in
731 crushable sands." *Can. Geotech. J*. 51(10), 1095-1110.
732 White, D.J. 2002. “An inverstigation into the behavior of pressed-in piles.” PhD thesis, Cambridge
733 University.
734 White, D.J., and Bolton, M.D. 2004. ”Displacement and strain paths during plane-strain model pile
735 installation in sand.” *Géotechnique* 54(6): 375-397.
736 White, D.J. and Lehane, B.M. 2004. "Friction fatigue on displacement piles in sand." *Géotechnique*
737 54(10): 645-658.
738 Wichtmann, T., Triantafyllidis, T. 2010. “On the influence of the grain size distribution curve on P-
739 wave velocity, constrained elastic modulus M_{max} and Poisson's ratio of quartz sands.” *Soil Dyn.*
740 *Earthq. Eng*. 30(8), 757-766.
741 Yang, Z.X., Gao, Y.Y., Jardine, R.J., Guo, W.B., and Wang, D. 2020. “Large deformation finite element
742 simulation of displacement pile installation experiments in sand.” *J. Geotech. Geoenviron. Eng.*
743 146(6), 04020044.
744 Yang, Z.X., Guo, W.B., Jardine, R.J., and Chow, F. 2017. "Design method reliability assessment from
745 an extended database of axial load tests on piles driven in sand." *Can. Geotech. J.* 54(1), 59-
746 74.
747 Yang, Z.X., Guo, W.B., Zha, F.S., Jardine, R.J., Xu, C.J., and Cai, Y.Q. 2015a. “Field behavior of driven
748 pre-stressed high-strength concrete piles in sandy soils.” *J. Geotech. Geoenviron. Eng*. 141(6),
749 04015020.

750 Yang, Z.X., Jardine, R.J., Guo, W.B., and Chow, F. 2015b. "A new and openly accessible database of
751 tests on piles driven in sands." *Géotechnique Lett*. 5(January – March), 12-20.
752 Yang, Z.X., Jardine, R.J., Guo, W.B., and Chow, F. 2015c. *A comprehensive database of tests on axially*
753 *loaded piles driven in sand*, Amsterdam, Netherlands: Press Elsevier.
754 Yang, Z.X., Jardine, R.J., Zhu, B.T., Foray, P., and Tsuha, C.H.C. 2010. "Sand grain crushing and
755 interface shearing during displacement pile installation in sand." *Géotechnique* 60(6), 469-482.
756 Yang, Z.X., and Pan, K. (2017). "Flow deformation and cyclic resistance of saturated loose sand
757 considering initial static shear effect." *Soil Dyn. Earthq. Eng*., 92, 68-78.
758 Yang, Z. X., Wen, Y. X., and Pan, K. 2019. "Previbration Signature on Dynamic Properties of Dry
759 Sand." *J. Test Eval.* 47(3), 2167-2192.
760 Yimsiri, S., Soga, K., Yoshizaki, K., Desari, G.R., and O'Rourke, T. D. 2004. "Lateral and upward soil-
761 pipeline interactions in sand for deep embedment conditions." *J. Geotech. Geoenviron, Eng.*
762 130(8), 830-842.
763 Zhang, C., Nguyen, G.D., and Einav, I. 2013. "The end-bearing capacity of piles penetrating into
764 crushable soils." *Géotechnique* 63(5), 341-354.
765 Zhang, C., Yang, Z.X., Nguyen, G.D., Jardine, R.J., and Einav, I. 2014. "Theoretical breakage
766 mechanics and experimental assessment of stresses surrounding piles penetrating into dense
767 silica sand." *Géotechnique Lett*. 4, 11-16.

Table 1 Index properties of #2Q-ROK sand

Specific gravity, G_s	D_{50}: mm	C_u	e_{max}	e_{min}	Silicon dioxide: %
2.65	0.75	1.43	0.998	0.668	99.0

Table 2 Summary of tests performed and results (D_r =82%)

Cell pressure (kPa)	Shearing resistance angle ψ' (°)	Dilatancy angles φ' (°)
100	23.0	39.86
150	22.5	39.54
200	21.8	39.42
300	20.6	39.27
400	17.3	39.01
500	16.5	38.51
600	12.6	38.03
700	10.6	37.26
800	7.5	36.80
1000	7.0	36.21

Table 3 (a) The final input of dilatancy and shearing resistance angles for different zones

Zone	p' (kPa)	ε_q^p (%)	Volumetric strain	ψ' (°)	φ' (°)
A	<300	0	< 0.1%	18.5	38.2
B	<500	0~15	0.1% ~ 2.1% (dilation)	17.4	37.3
C	500~1700	5~10	3.6% ~ 19.1% (dilation)	4.1	33.8
D	1700~2500	10~15	0 ~ 12.4% (dilation)	1.2	32.4
E	>=2500	>=15	0 ~ 10.3% (compression)	0	32.1
F	<500	>=15	5.9% ~ 35.8% (dilation)	0	32.1

(b) The final input of young's modulus for different zones

Zone	E_{12}（%）	p' (kPa)	Young's moduli (MPa)
1	< 0.001	< 50	156
2	0.001~ 0.02	< 100	125
3	0.02 ~ 0.1	< 300	88
4	0.1~1	< 500	46
5	>= 10	>=1500	30
6	> 10	< 1000	25

(c) Other input sand parameters for simulation

γ (kN/m^3)	Poisson's ratio ν	c (kPa)
15.36	0.25	0

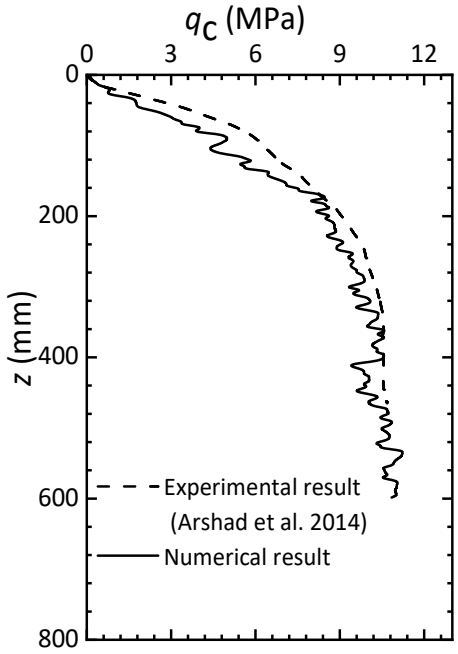


Fig. 1 CPT profiles for calibration chamber experiments

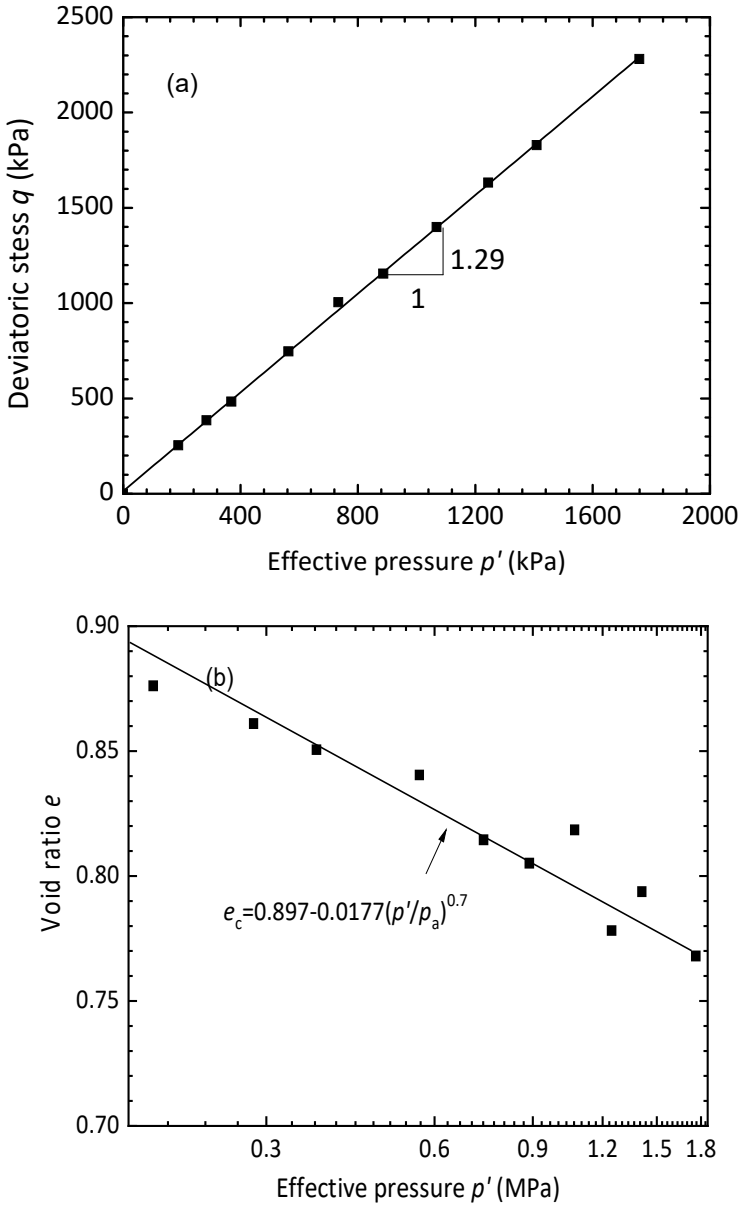


Fig. 2 Critical state relationships for #2Q-ROK sand

(a) p'-q plane; (b) e-$(p')^{0.7}$ plane

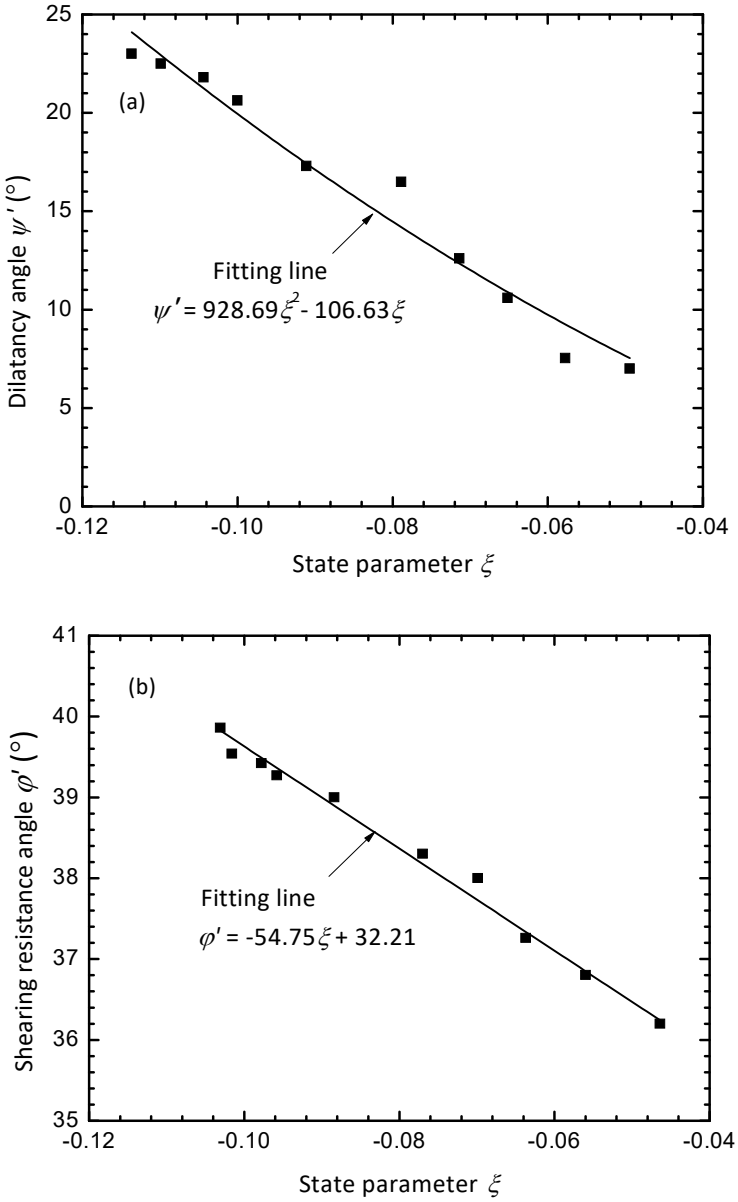


Fig. 3 Relationship between dilatancy angle ψ', shearing resistance angle φ' and state parameter ξ
(a) dilatancy angle; (b) shearing resistance angle

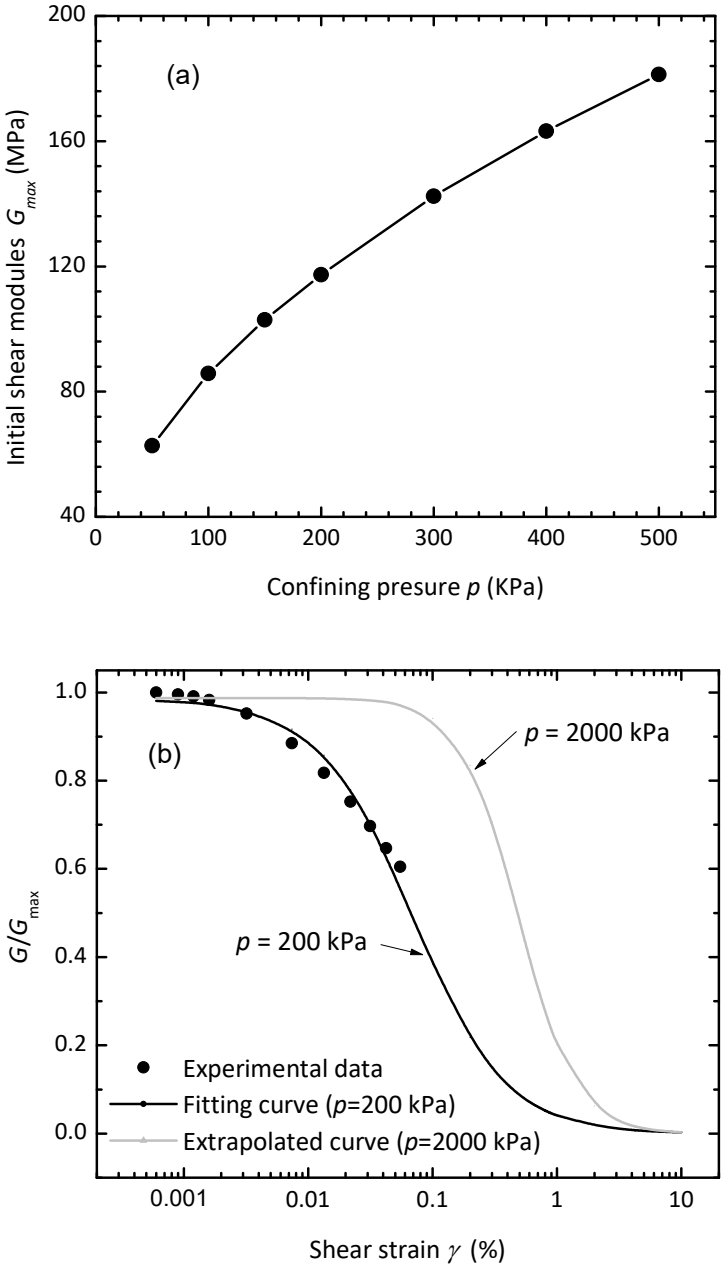


Fig. 4 Results of resonant column tests

(a) Initial shear modules measured by the resonant column tests (D_r=82%);

(b) Reduction curves in different confining pressure

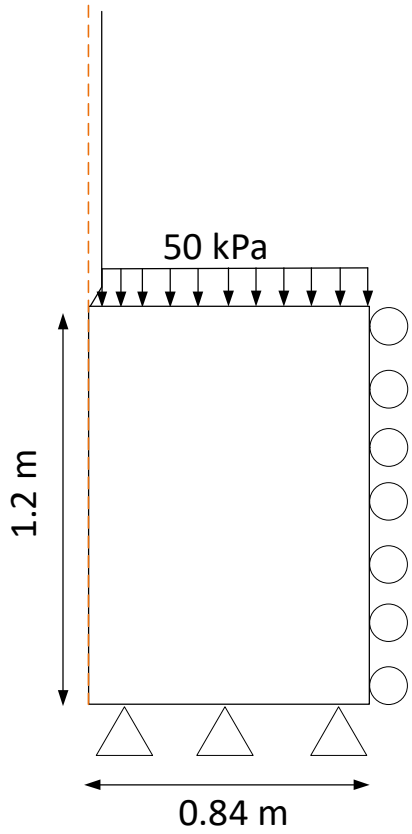


Fig. 5 Geometry and boundary conditions of the numerical model

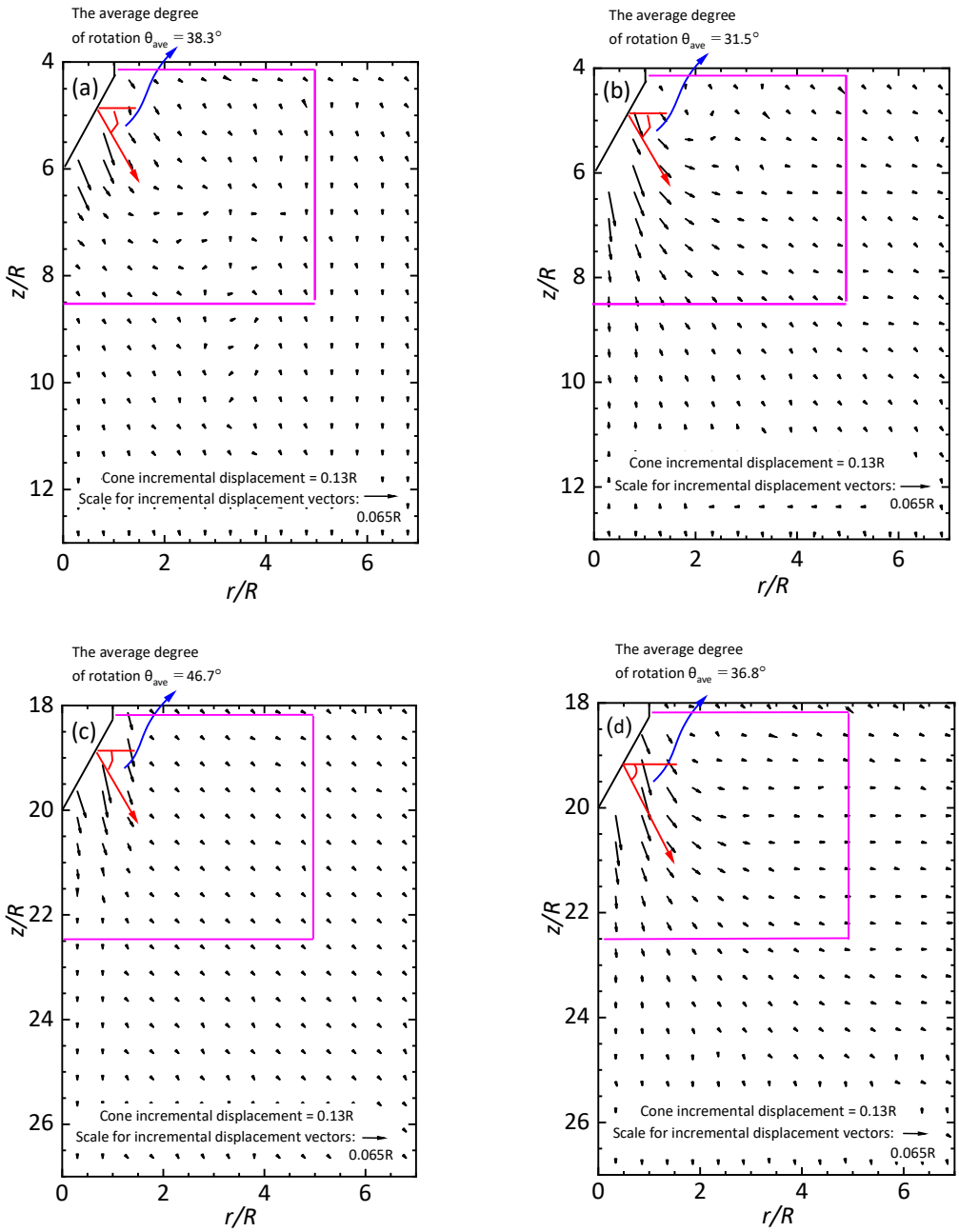


Fig. 6 Soil displacement patterns at various normalized tip positions
(a) z/r=6 of numerical results; (b) z/r=6 of experimental results;
(c) z/r=20 of numerical results; (d) z/r=20 of experimental results

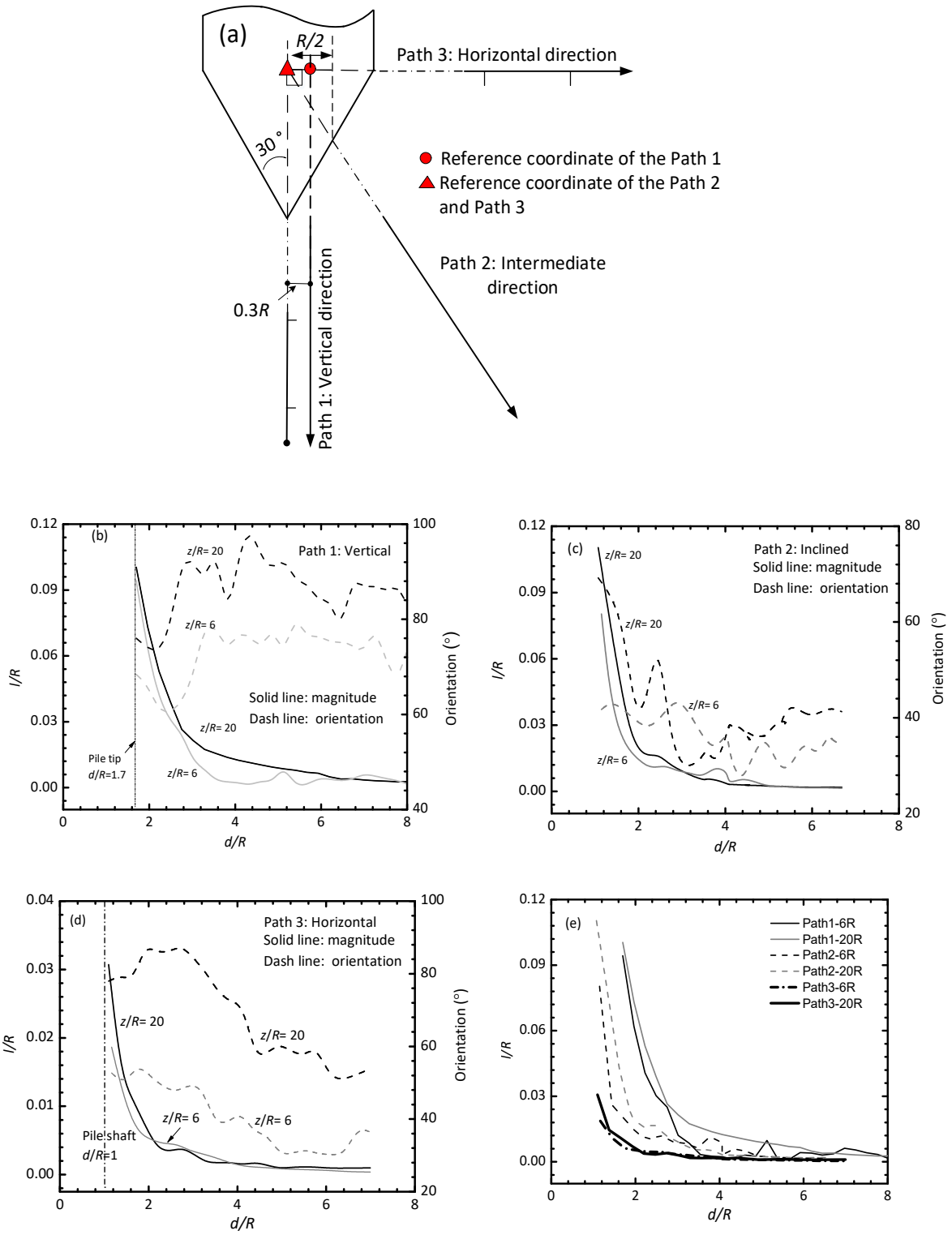


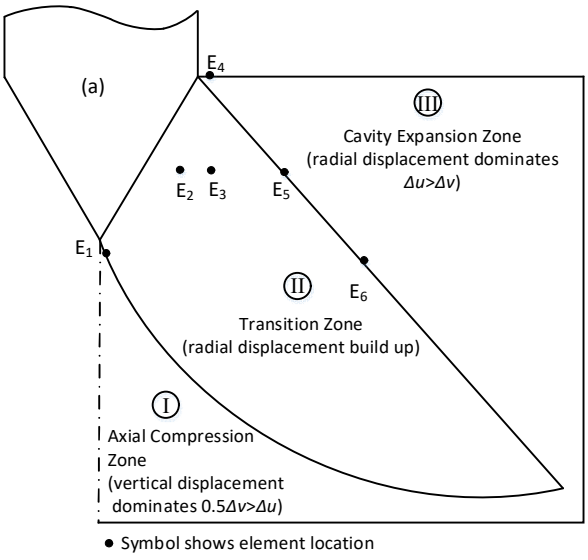
Fig. 7 Numerical predictions for magnitudes and angles along three paths of the displacement increments at two penetration depths

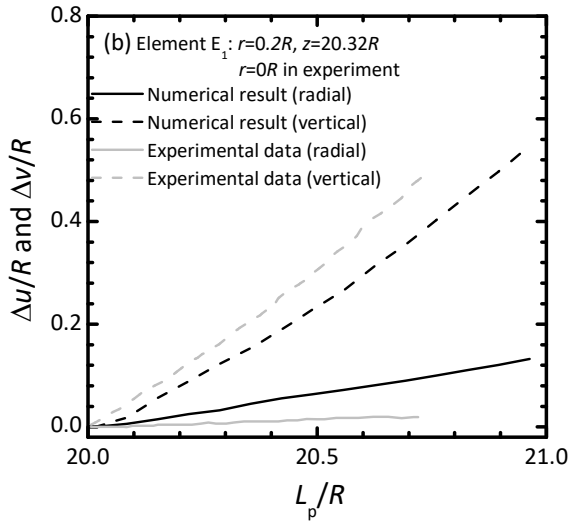
(a) Schematic of paths from the cone tip; (b) The results along the vertical direction (Path 1);

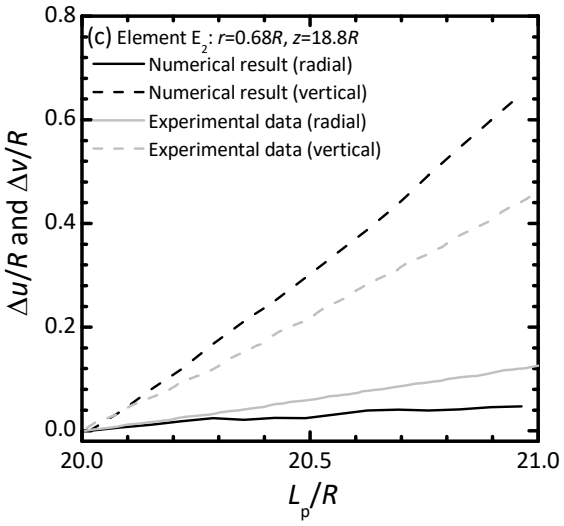
(c) The results along the intermediate direction (Path 2);

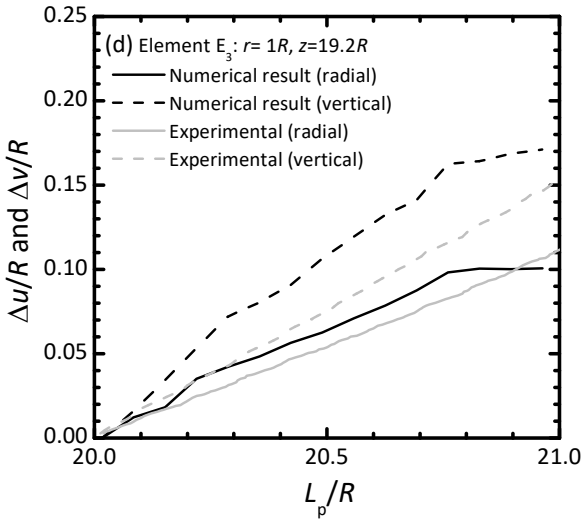
(d) The results along the horizontal direction (Path 3);

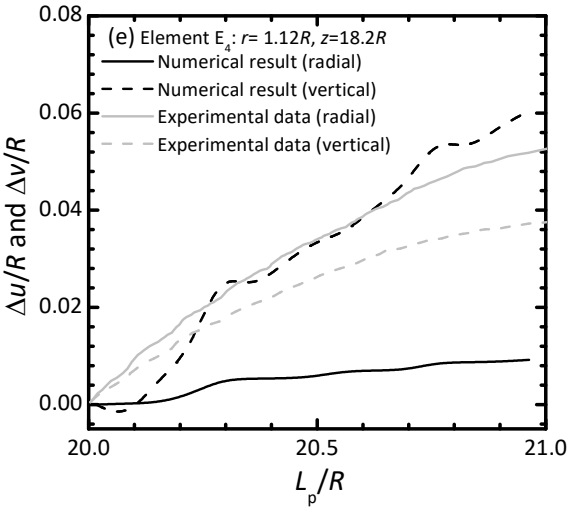
(e) The summary of magnitudes of displacement vectors


(a)
E4
III
Cavity Expansion Zone
(radial displacement dominates
Δu>Δv)
E2
E3
E5
E1
II
E6
Transition Zone
(radial displacement build up)
I
Axial Compression
Zone
(vertical displacement
dominates 0.5Δv>Δu)
Symbol shows element location


(b) Element E1: r=0.2R, z=20.32R
r=0R in experiment
Numerical result (radial)
Numerical result (vertical)
Experimental data (radial)
Experimental data (vertical)
Δu/R and Δv/R
Lp/R
0.0
0.2
0.4
0.6
0.8
20.0
20.5
21.0


(c) Element E2: r=0.68R, z=18.8R
Numerical result (radial)
Numerical result (vertical)
Experimental data (radial)
Experimental data (vertical)
Δu/R and Δv/R
Lp/R
0.0
0.2
0.4
0.6
0.8
20.0
20.5
21.0


(d) Element E3: r= 1R, z=19.2R
Numerical result (radial)
Numerical result (vertical)
Experimental (radial)
Experimental (vertical)
Δu/R and Δv/R
Lp/R
0.00
0.05
0.10
0.15
0.20
0.25
20.0
20.5
21.0


(e) Element E4: r= 1.12R, z=18.2R
Numerical result (radial)
Numerical result (vertical)
Experimental data (radial)
Experimental data (vertical)
Δu/R and Δv/R
Lp/R
0.00
0.02
0.04
0.06
0.08
20.0
20.5
21.0

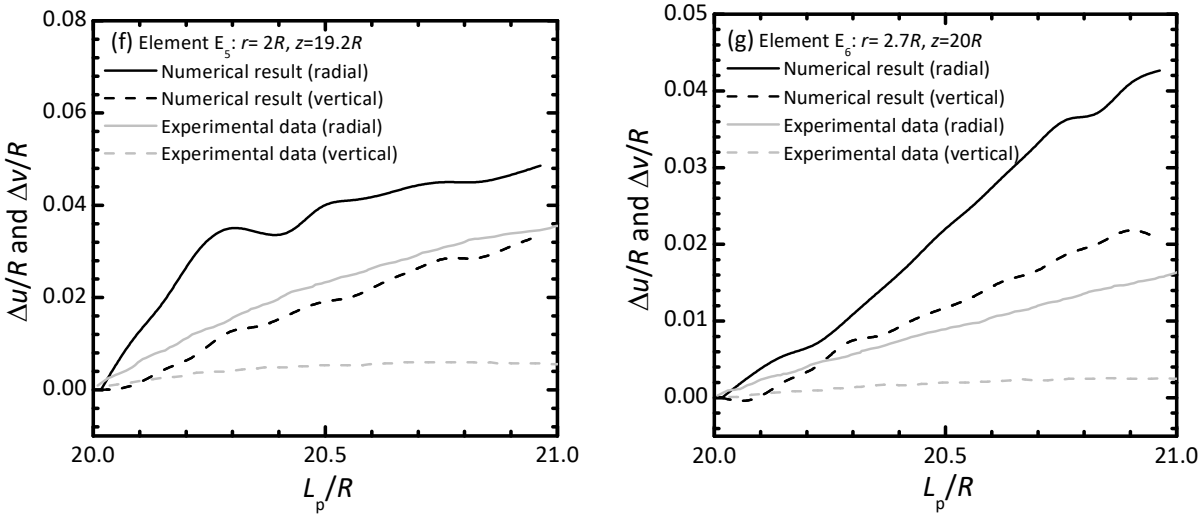


Fig. 8 Characterization of displacement zones

(a) Displacement zones with the proposed criterion to partition the zones;

(b)~(g) Evolution of radial and vertical displacement change for 1 *R* penetration in different zones

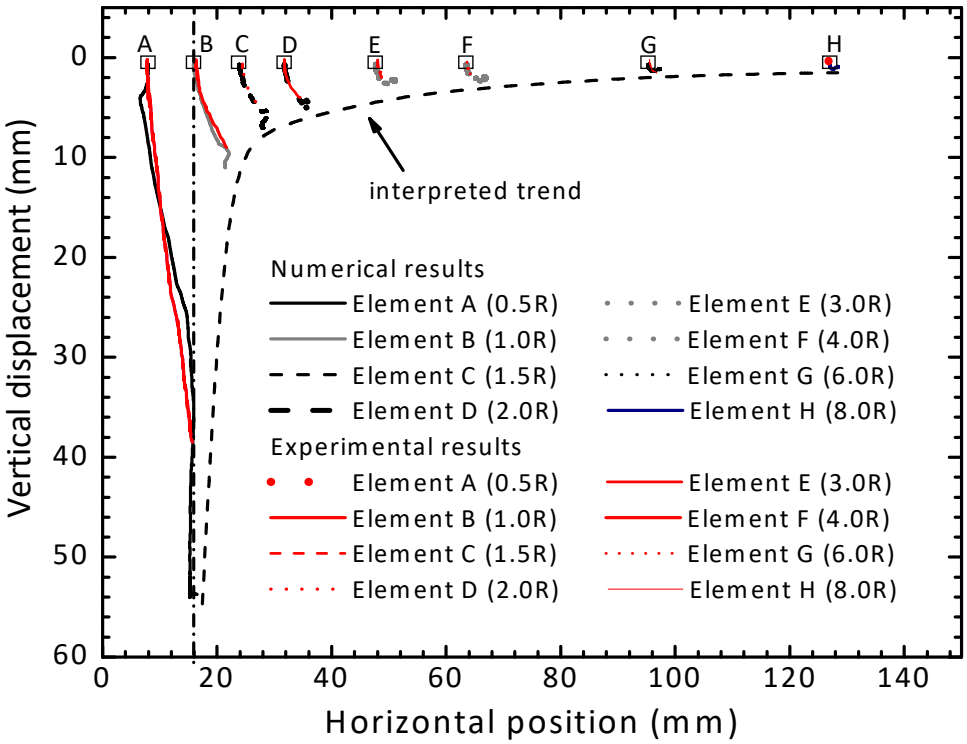


Fig. 9 Displacement paths during cone penetration from z=0R to z= 30R for different soil elements.

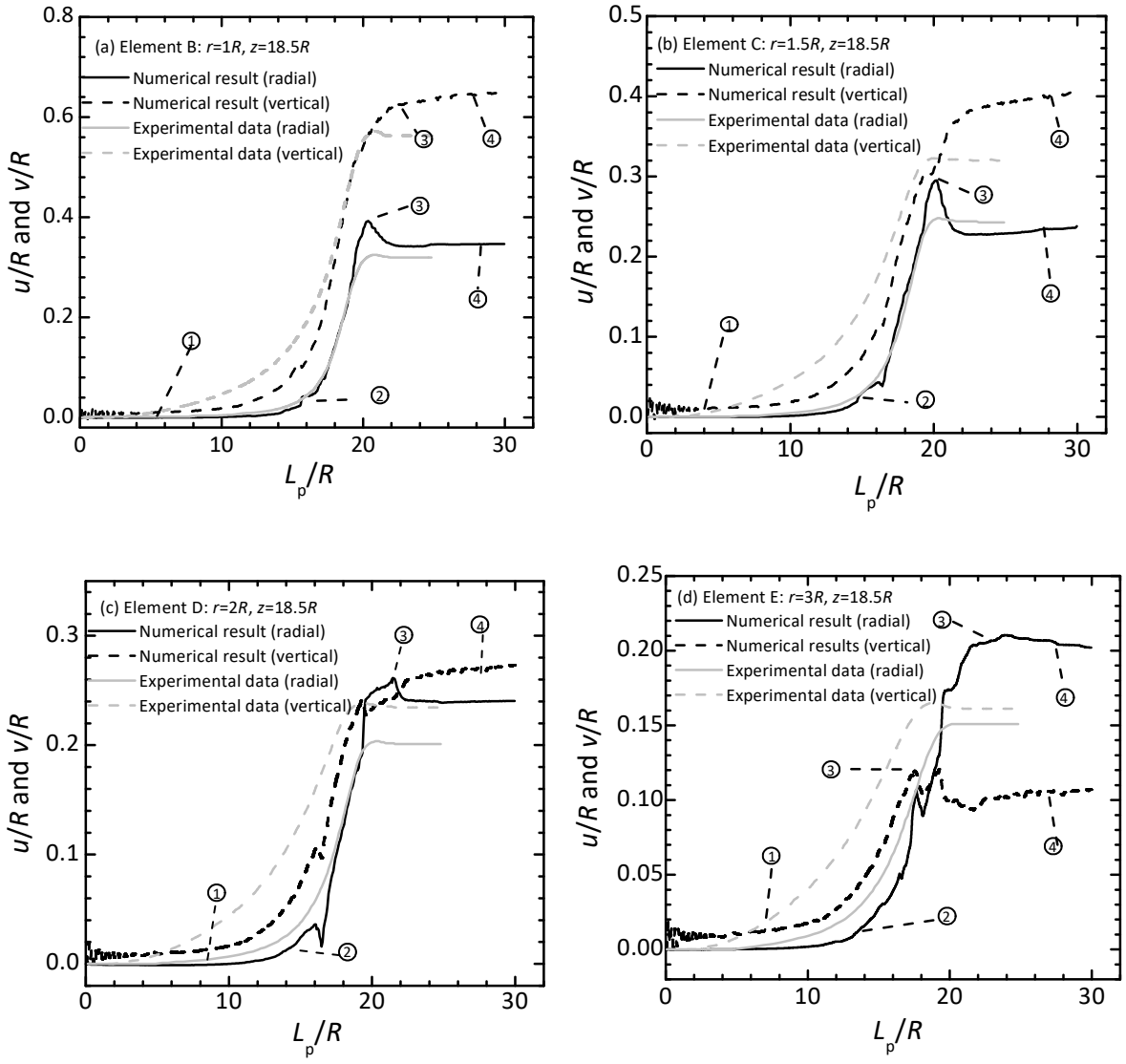


Fig. 10 Evolution of normalized radial and vertical displacements of soil elements at different locations during the cone penetration

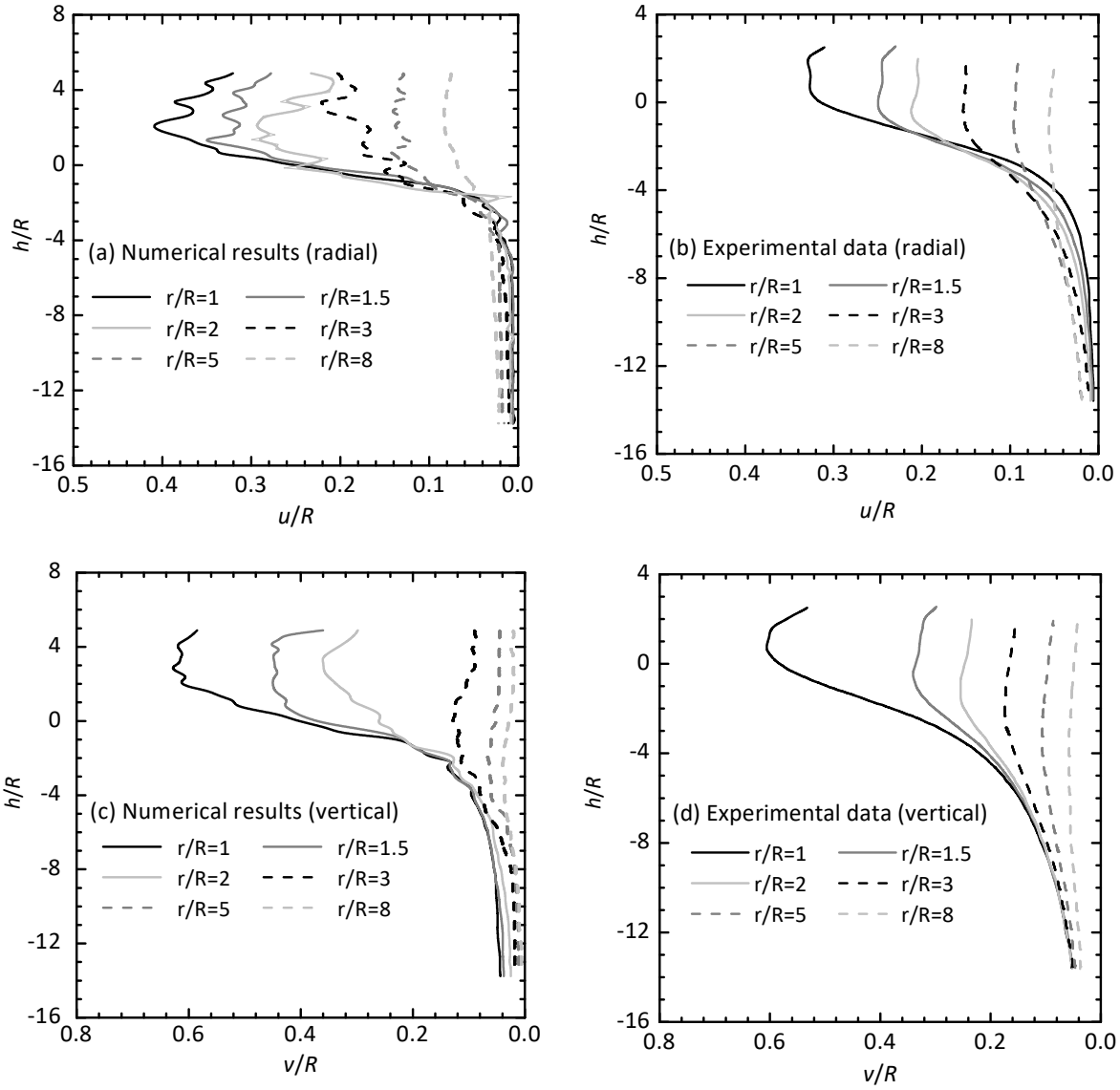


Fig. 11 Displacement path below the cone tip when the cone is at z= 20R

(a) Radial displacements-numerical results; (b) Radial displacements-experimental results

(c) Vertical displacements-numerical results; (d) Vertical displacements-experimental results

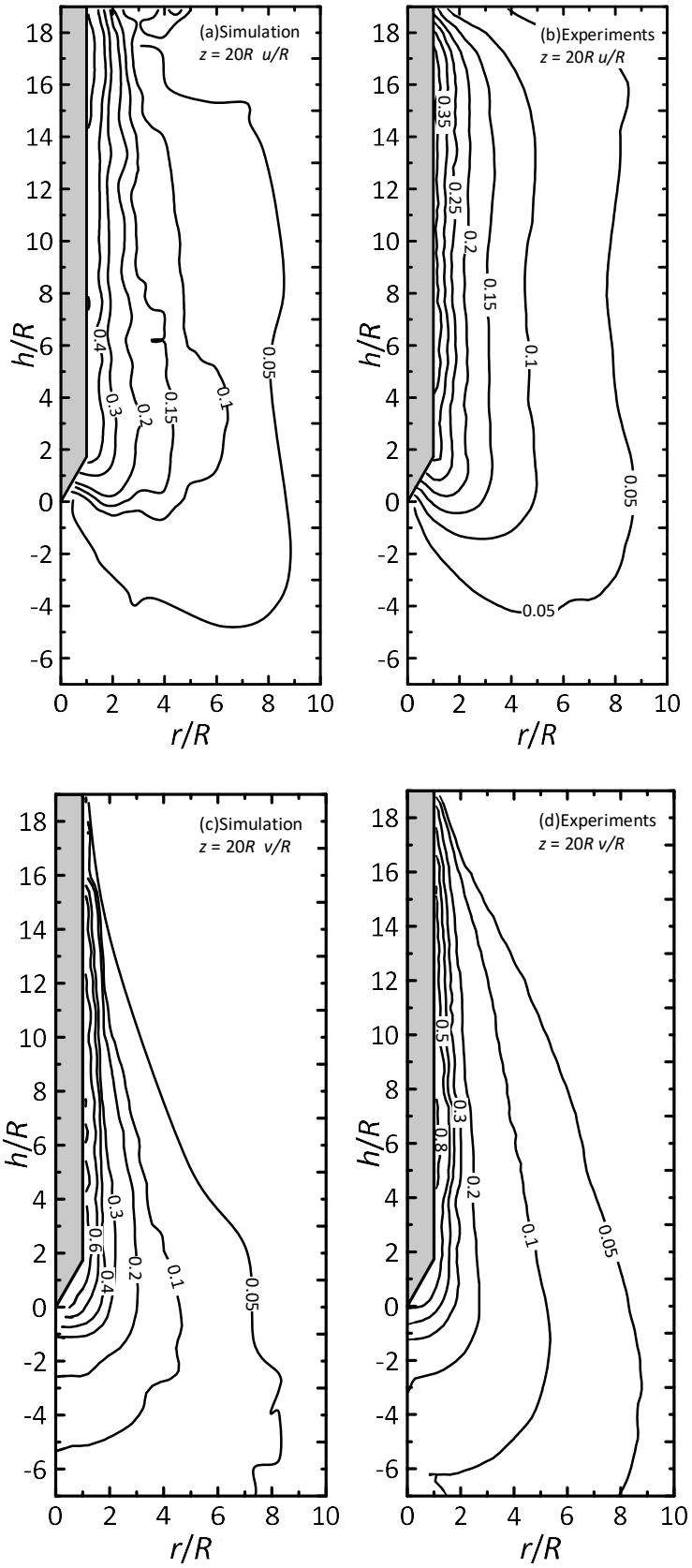
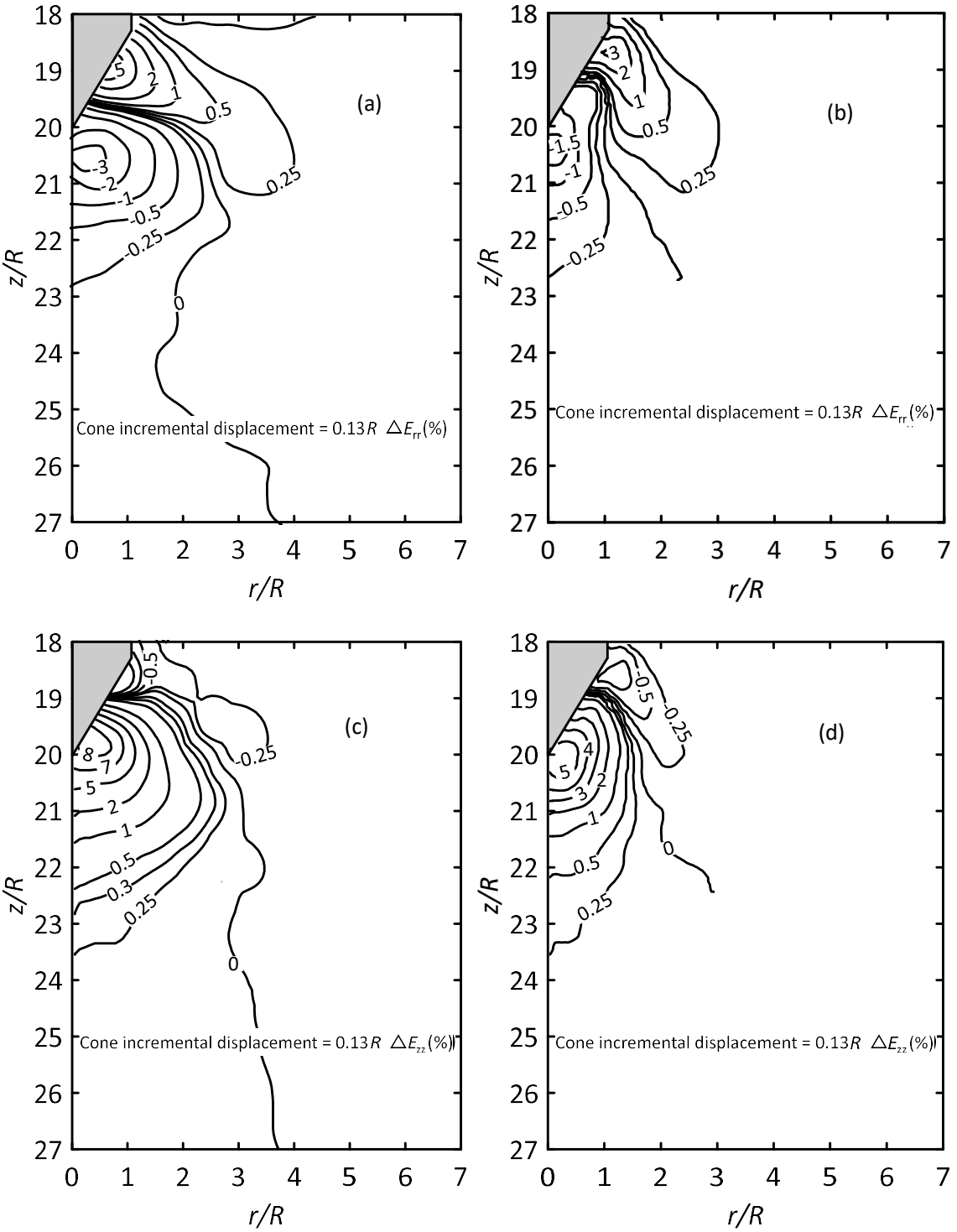


Fig. 12 Normalized displacements after cone penetration to approximately z= 20R.
(a) Radial displacement-numerical results; (b) Radial displacement-experimental results;
(c) Vertical displacement-numerical results; (d) Vertical displacement-experimental results


(a)
Cone incremental displacement = 0.13R △E_rr(%)
(b)
Cone incremental displacement = 0.13R △E_rr(%)
(c)
Cone incremental displacement = 0.13R △E_zz(%)
(d)
Cone incremental displacement = 0.13R △E_zz(%)
z/R
r/R

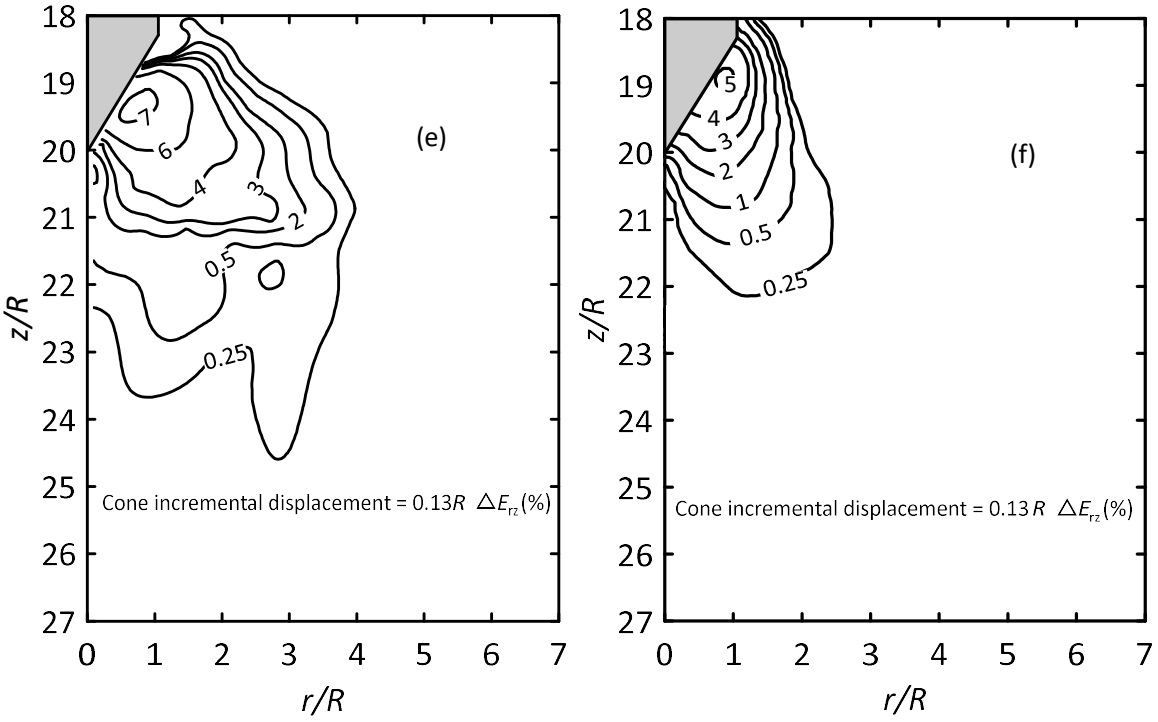
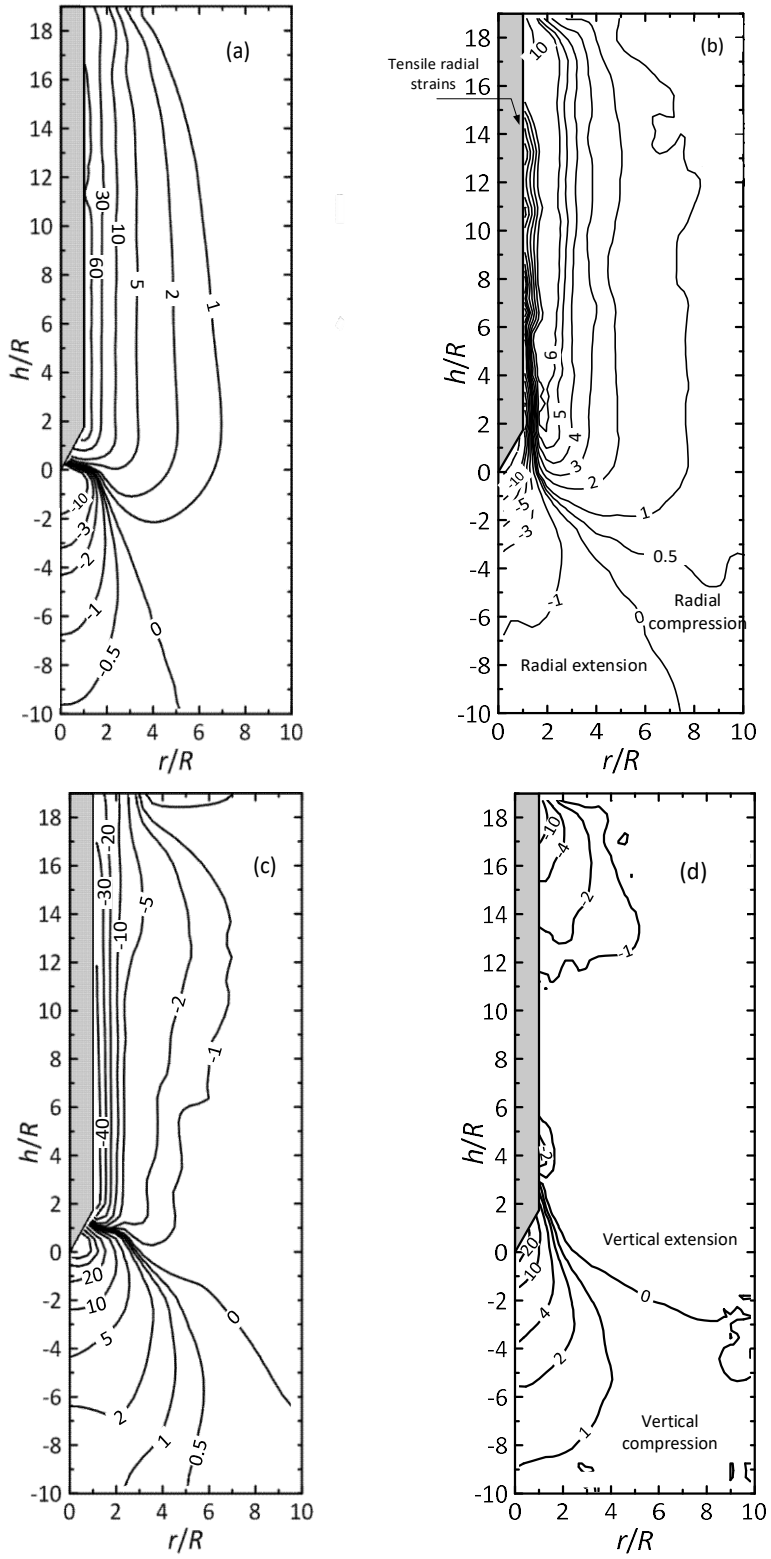


Fig. 13 Components of strain increments at *z/R*= 20.

(a) Radial strain increments-numerical results (b) Radial strain increments-experimental results;

(c) Vertical strain increments-numerical results; (d) Vertical strain increments-experimental results

(e) Shear strain increments-numerical results; (f) Shear strain increments-experimental results


(a)
(b)
(c)
(d)
Tensile radial strains
Radial compression
Radial extension
Vertical extension
Vertical compression
h/R
r/R

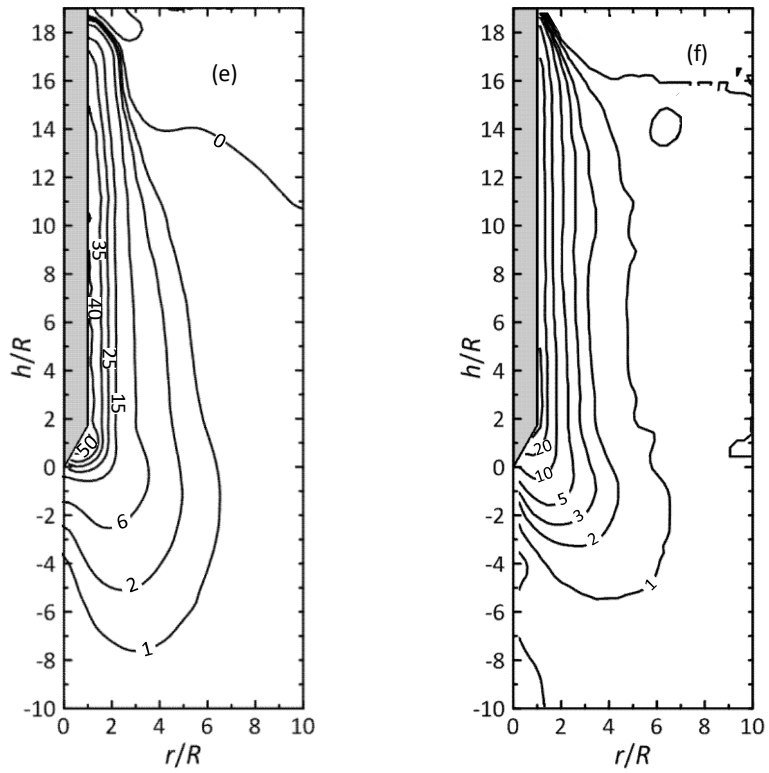


Fig. 14 Post installation, cumulative strain field after penetration from z=0R to z= 20R. (a) Numerical radial strain; (b) Experimental radial strain; (c) Numerical vertical strain; (d) Experimental vertical strain; (e) Numerical shear strain; (f) Experimental shear strain

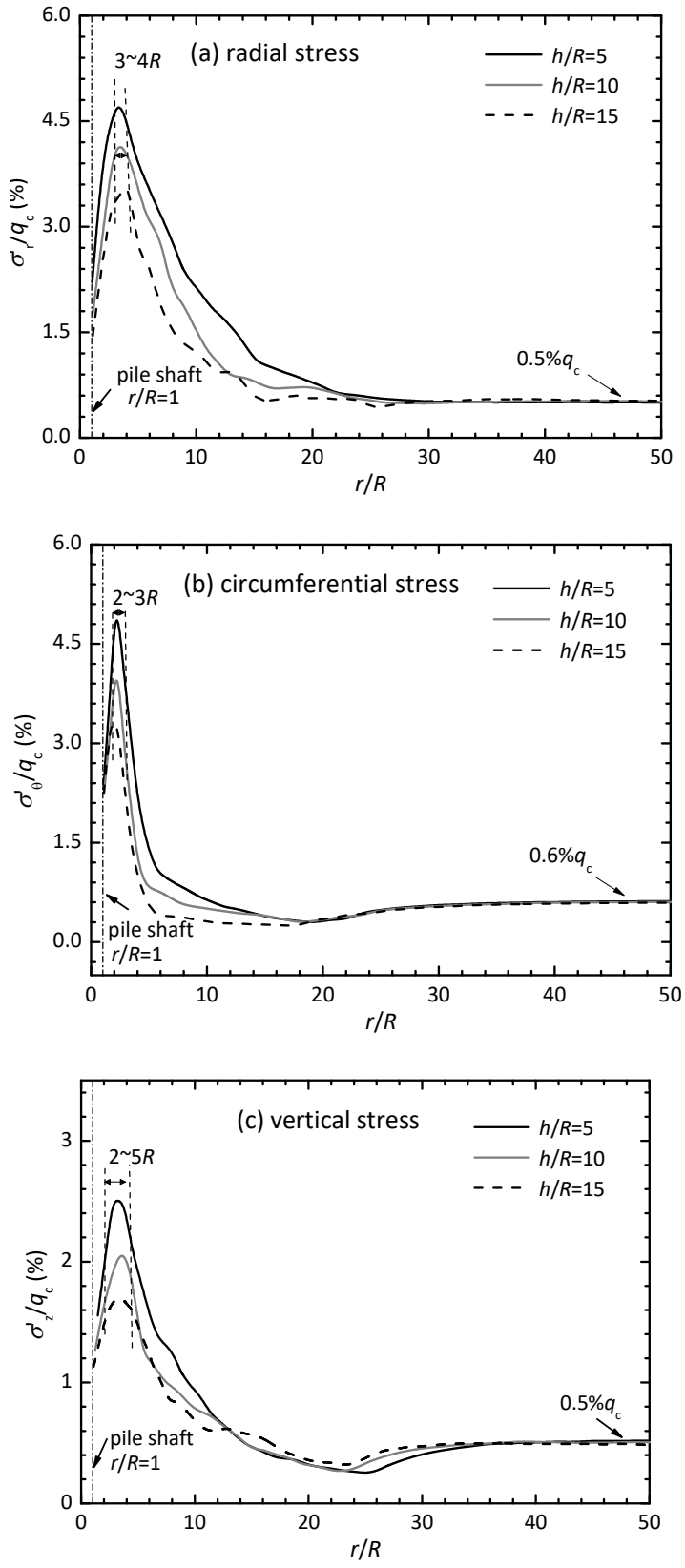


Fig. 15 Numerical results of stresses acting above tip (h=R > 5) at the end of the penetration: (a) Radial stress; (b) Circumferential stress; (c) Vertical stress

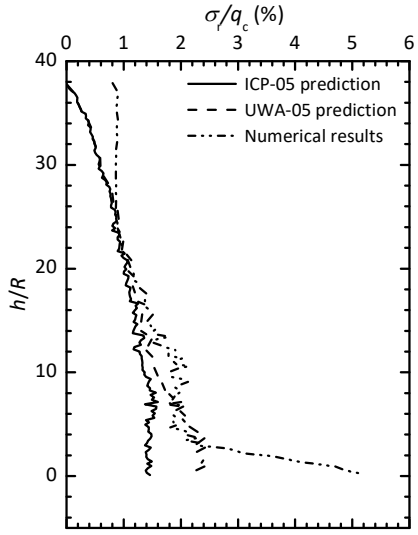


Fig. 16 Shaft radial stresses normalized by q_c at the depth of 600 mm